OPEN ACCESS

University of BRISTOL

Mahoney, E. J. D., Ashfold, M. N. R., Mankelevich, Y. A., & Truscott, B. S. (2020). Optical Emission Imaging and Modelling Investigations of Microwave Activated SiH_4/H_2 and $SiH_4/CH_4/H_2$ Plasmas. *Journal of Physical Chemistry A*, *124*, 5109-5128. https://doi.org/10.1021/acs.jpca.0c03396

Peer reviewed version

Link to published version (if available):
10.1021/acs.jpca.0c03396

Link to publication record in Explore Bristol Research
PDF-document

This is the author accepted manuscript (AAM). The final published version (version of record) is available online via American Chemical Society at https://pubs.acs.org/doi/abs/10.1021/acs.jpca.0c03396 . Please refer to any applicable terms of use of the publisher.

University of Bristol - Explore Bristol Research
General rights

This document is made available in accordance with publisher policies. Please cite only the published version using the reference above. Full terms of use are available:
http://www.bristol.ac.uk/red/research-policy/pure/user-guides/ebr-terms/

Optical Emission Imaging and Modelling Investigations of Microwave Activated SiH_4/H_2 and $SiH_4/CH_4/H_2$ Plasmas

Edward J.D. Mahoney,[1,2] Alim K.S.K. Lalji,[1] John W.R. Allden,[1] Benjamin S. Truscott,[3] Michael N.R. Ashfold [1]* and Yuri A. Mankelevich [4]*

[1] School of Chemistry, University of Bristol, Bristol, U.K. BS8 1TS

[2] Centre for Doctoral Training in Diamond Science and Technology, University of Warwick, Gibbet Hill Road, Coventry, U.K., CV4 7AL

[3] Element Six Ltd., Global Innovation Centre, Fermi Avenue, Didcot, U.K. OX11 0QR.

[4] Skobeltsyn Institute of Nuclear Physics, Lomonosov Moscow State University, Leninskie gory, Moscow, 119991, Russia

ABSTRACT

Silicon is a known trace contaminant in diamond grown by chemical vapor deposition (CVD) methods. Deliberately Si-doped diamond is currently attracting great interest because of the attractive optical properties of the negatively charged silicon-vacancy (SiV^-) defect. This work reports in-depth studies of microwave activated H_2 plasmas containing trace (10-100 ppm) amounts of SiH_4, with and without a few % of CH_4, operating at pressures and powers relevant for contemporary diamond CVD, using a combination of experiment (spatially resolved optical emission (OE) imaging) and two-dimensional plasma chemical modelling. Key features identified from analysis and modelling of the OE from electronically excited H, H_2, Si, and SiH species in the dilute Si/H plasmas include (i) fast H-shifting reactions ensure that Si atoms are the most abundant silicon-containing species throughout the entire reactor volume, (ii) the low ionization potentials of all SiH_x ($x \leq 4$) species and efficient ion conversion reactions ensure that even trace SiH_4 additions cause a change in the dominant ions in the plasma volume (from H_3^+ to SiH_x^+), with consequences for electron-ion recombination rates and ambipolar diffusion coefficients and (iii) the total silicon content in the reactor volume can be substantially perturbed by silicon deposition and H atom etching reactions at the reactor walls. The effects of adding trace amounts of SiH_4 to a pre-existing C/H plasma are shown to be much less dramatic, but include (i) a Si substrate or fused silica components within the reactor is a ready (unintended) source of gas phase Si-containing species, (ii) OE from electronically excited Si atoms should provide a reliable measure of the Si content in the hot plasma region and (iii) Si atoms and/or SiC_2 species are the most abundant gas phase Si-containing species just above the growing diamond surface and thus the most likely carriers of the silicon incorporated into CVD diamond.

1. INTRODUCTION

The fraction of diamond appearing on the world market that is grown in laboratories is increasing annually. Two laboratory-based methods dominate the supply of synthetic diamonds – high pressure high temperature (HPHT) synthesis and chemical vapour deposition (CVD). CVD methods appeared more recently but are claiming an ever-increasing market share. Most contemporary diamond CVD employs microwave- (MW-) activated dilute carbon/hydrogen (typically CH_4/H_2) plasmas,[1] and the method is well suited to growing doped diamond by controlled addition of a suitable precursor to the source gas mixture (*e.g*. diborane [2] or silane,[3-45] if B- or Si-doped diamond is the target material). The gas phase and plasma chemistry that underpins diamond CVD is by now quite well understood, through a combination of experiments (*e.g*. laser absorption and/or optical emission spectroscopy measurements [6-9] of the densities of selected gas phase species in their ground and/or excited states) and complementary plasma modelling.[6-8,10]

Silicon is a common trace element in CVD-grown diamond,[11-18] arising either adventitiously – by etching from the silicon substrate on which diamond is commonly grown or from silica windows or walls of the MW reactor during hydrogen termination and/or growth of diamond – or by design if, for example, SiH_4 is added to the process gas mixture. The silicon-vacancy (SiV) defect, wherein a Si atom is located in a site within the diamond lattice corresponding to two missing carbon atoms (*i.e*. in an interstitial site within a divacancy, often termed a split vacancy),[19-22] is currently attracting much interest, both in its neutral and negatively charged form. The SiV^- defect shows a zero phonon line at a wavelength λ = 738 nm, which is sufficiently stable, narrow (reflecting the weak electron-phonon coupling) and bright (10% luminescence quantum yield at room temperature) to be an attractive single photon source in quantum technologies [23-34] and, when incorporated in nanodiamond particles, to serve as a fluorescent marker in bioimaging applications [35,36] and as a nanothermometer.[37] The neutral SiV^0 defect is less well characterised but is likely to be the more prevalent form in lightly doped high quality diamond. It too shows a sharp zero phonon line (at 946 nm), exhibits long spin lifetimes and holds considerable promise for future quantum technologies.[38]

Here we present a comprehensive combined experimental (spatially and spectrally resolved optical emission (OE) imaging of Si*, SiH*, H*, H_2* and, when appropriate, CH* and C_2* species – with the asterisk in each case indicating that the species is in an excited electronic state) – and 2-D plasma chemical modelling study of MW activated Si/H and Si/C/H plasmas operating over ranges of powers and pressures relevant for contemporary diamond CVD. This caveat is important, since activated Si/H and Si/C/H gas mixtures have already attracted attention in the context of plasma enhanced CVD of, respectively, amorphous silicon (a-Si) and amorphous silicon carbide (a-SiC) layers for solar cell applications.[39,40] Compared with diamond CVD, most such silicon-related growth involves much lower temperature and pressure plasmas [41-44] (with correspondingly higher electron temperatures [43]). For

completeness, we also note reports of a-Si growth using direct MW-activated SiH_4/Xe plasmas,[45] of a-SiC growth using indirect MW-activated Si/C/H plasmas at low (~1 Torr) pressures,[46] of the co-deposition of diamond and SiC in activated Si/C/H mixtures,[47-49] and prior experimental and computational studies of Si/H [50,51] and Si/C/H [52,53] kinetics at gas temperatures relevant to the present work. The experimental set-up and procedures are first summarized. This is followed by sections devoted to measurements and 2-D(r, z) modelling of, first, MW-activated Si/H and then Si/C/H gas mixtures (where r and z are, respectively, the radial and axial distances from the centre of the top surface of the substrate on which deposition occurs). Comparisons between the experimental observations and model outputs allow us to rationalise many of the observed (spatially dependent) variations in emission intensities with changes in process conditions, to recognise discernible wall-dependent effects in the case of Si/H plasmas and, in the case of Si/C/H plasmas, to identify the most abundant Si-containing species in the immediate vicinity of the substrate on which the diamond grows.

2. EXPERIMENTAL

The CVD reactor, the MW power supply, the gas regulation and supply and the set-up for OE imaging from the hot plasma region have all been described previously,[54,55] and we here focus on details specific to the present study. The silane precursor was obtained as a 0.1% SiH_4 in H_2 mixture (sourced from CK Special Gases Limited, 99.9995% stated purity). Table 1 lists the atomic and diatomic species, levels and emissions monitored in this work, and the sources for the necessary spectroscopic data.[54,56-63]

Insert Table 1 near here

The OE imaging methods were similar to those reported for our recent studies of C/H plasmas [55] except for the substrate (a 3 mm thick, 32 mm diameter Mo disc seated on a thin spacer wire of diameter, d_{wire} = 0.01″ bent into a circle), the image accumulation time (which for all data reported here was, or was equivalent to, 50 s), and that all emissions at wavelengths $\lambda < 270$ nm were monitored via their (much weaker) second order diffraction.

Base conditions for the SiH_4/H_2 plasma studies were: MW power P = 1.5 kW, total gas pressure p = 150 Torr, and respective flow rates of hydrogen $F(H_2)$ = 300 standard cm^3 per minute (sccm) and of the 0.1% (or 1000 parts per million (ppm)) SiH_4 in H_2 gas mixture $F(SiH_4/H_2)$ = 15 sccm. The effects of changing process conditions were explored by varying one of these parameters at a time, holding all others at their base value. The wait time before resuming data collection after any change in process conditions was ≥6 min. – the approximate residence time for the gas in the reactor – and the parameter space explored spanned: $0 \leq F(SiH_4/H_2) \leq 40$ sccm, $50 \leq p \leq 275$ Torr and $0.7 \leq P \leq 1.85$ kW. A further series of OE imaging experiments on Si/H plasmas employed MW-activated H_2 and H_2/Ar plasmas operating at base p and P with, respectively, $F(H_2)$ = 300 sccm and with $F(H_2) = F(Ar)$ = 300 sccm,

with the substrate completely covered by a thin (0.7 mm thick) polished silicon wafer and held off the water-cooled reactor base plate by a thinner spacer wire (d_{wire} = 0.002″).

The $SiH_4/CH_4/H_2$ plasma studies employed the same base P (1.5 kW) and p (150 Torr), along with $F(H_2)$ = 270 sccm, $F(CH_4)$ = 19 sccm and twice the input silane fraction (*i.e.* $F(SiH_4/H_2)$ = 30 sccm). All emissions from the Si/C/H plasmas were investigated over the same ranges of p, P and $F(SiH_4)$ – again, varying the parameters in turn with all others maintained at their base values. The effects of varying the methane flow rate were investigated also, over the range $0 \leq F(CH_4) \leq 30$ sccm. For this one variable, $F(H_2)$ was adjusted in a compensatory manner so that the total gas flow F_{total} remained constant. The air leak rate (estimated from measuring the pressure rise from base vacuum over a fixed period of time) was estimated to be ~0.25 ppm under base operating conditions. Thus, for all the experiments reported here, the main source of impurity was likely to be the input gases themselves.

3. RESULTS and DISCUSSION

3.1 Si/H Plasmas

This Section reports the different Si* and SiH* emission spectra from MW-activated dilute Si/H plasmas, and the ways in which the spatial distributions and relative intensities of these emissions vary with changes in process conditions. These trends are then compared with 2-D plasma chemical modelling results. These comparisons suggest that electron impact excitation (EIE) is one important source of the observed triplet and singlet Si* (henceforth ^{3}Si* and ^{1}Si*) and SiH* emissions, but, as in our recent studies of CH* emissions from MW-activated CH_4/H_2 plasmas,[55] the present data can only be satisfactorily explained by assuming that both EIE and chemiluminescent (CL) reactions contribute to the observed emissions.

3.1.1. Optical Emission Images and Spectral Analysis

Figures 1(a) and 1(b) show, respectively, a spatially-resolved false colour $I_{em}(\lambda, z)$ image of the emission intensities from a Si/H plasma operating under base conditions in the wavelength range $372 \leq \lambda \leq 447$ nm and a spatial range $-3 \leq z \leq 27$ mm, where z = 0 mm defines the top of the 3 mm thick substrate, and the $I_{em}(\lambda)$ plot obtained by summing all emission intensity in the range $10.5 \leq z \leq 12$ mm for the wavelength range $410 \leq \lambda \leq 425$ nm. The experimentally measured spectrum in Figure 1(b) includes several overlapping emissions. The simulation of the SiH(A→X), Δv = 0 bands was obtained using the PGOPHER software,[64] the appropriate spectroscopic constants for the $A^2\Delta$ and $X^2\Pi$ states,[57] a Gaussian transition linewidth of 0.1 nm (full width half maximum, FWHM, to mimic the instrumental resolution) and a best-fit rotational temperature T_{rot} = 2450±200 K. The residual still shows rich structure, almost all of which is attributable to H_2* emissions, while the pink trace shows the corresponding emission spectrum from a bare H_2 plasma operating measured under the same conditions of p, P, *etc* and for the

same z range. We return to assign the one remaining feature (at $\lambda \sim 411.6$ nm) after considering the Si* transitions in Figure 2.

Figures 2(a) and 2(c) show false colour $I_{em}(\lambda, z)$ images of the emission intensities from the same Si/H plasma in the wavelength ranges $252 \leq \lambda \leq 327$ nm and $463 \leq \lambda \leq 534$ nm. The most prominent line in the former is the $3s^2 3p4s \rightarrow 3s^2 3p^2$; $^1P_1{}^o \rightarrow {}^1D_2$ transition at $\lambda = 288.16$ nm, the corresponding $I_{em}(\lambda)$ plot for which (obtained by summing all emission intensity in the range $10.5 \leq z \leq 12$ mm) is shown on an expanded wavelength scale in Figure 2(b). The related $3s^2 3p4s \rightarrow 3s^2 3p^2$; $^1P_1{}^o \rightarrow {}^1S_0$ transition (*i.e.* from the same upper state to the higher energy metastable singlet state) is evident in Figure 1(a) at $\lambda = 390.55$ nm. Nine lines are clearly visible in the optical emission image shown in Figure 2(c) and the corresponding $I_{em}(\lambda)$ plot obtained by summing all emission intensity in the range $10.5 \leq z \leq 12$ mm is shown on an expanded wavelength scale in Figure 2(d). One of these lines is the H Balmer-β transition at $\lambda = 486.13$ nm. The others can all be assigned to Si* transitions appearing in second order (*i.e.* at twice their true UV wavelength). The six lines in the range $250.69 \leq \lambda \leq 252.85$ nm are the various spin-orbit components of the $^3P^o \leftrightarrow {}^3P$ transition listed in Table 1, while the lines at 243.52 nm and 263.13 nm can be assigned to, respectively, the $3s^2 3p3d \rightarrow 3s^2 3p^2$; $^1D_2{}^o \rightarrow {}^1D_2$ and $^1P_1{}^o \rightarrow {}^1S_0$ transitions. As noted above, one line in the SiH_4/H_2 plasma emission spectrum at a (nominal) wavelength $\lambda \sim 411.6$ nm (black trace in Figure 1(b)) has not been assigned up to this point. It is most logically attributed to the $3s^2 3p5s \rightarrow 3s^2 3p^2$; $^1P_1{}^o \rightarrow {}^1D_2$ transition at 205.81 nm, appearing in second order.

3.1.2. Measured Si*, SiH*, H* and H_2* Emission Intensities with Changing Process Conditions

Figure 3 shows the $I_{em}(z)$ distributions of H_2*(d−a), H* (Balmer-γ), three different Si* and the SiH* emissions, recorded under base conditions. The Si* lines sample both singlet (*i.e.* the 288.16 and 390.55 nm lines) and triplet (*i.e.* the sextet of lines in the range $250.69 \leq \lambda \leq 252.85$ nm) excited states and the distributions shown in Figure 3 (each of which have been normalized to have the same peak intensity) are derived from the areas of the respective singlet lines and the summed intensities of all six triplet lines in the corresponding $I_{em}(\lambda)$ spectra. Henceforth these will be distinguished as $I_{em}(^1Si^*)$ and $I_{em}(^3Si^*)$ with, in the former case, the wavelength specified if relevant. The H_2* emission intensities were derived by summing the intensities of the well-resolved Q(1)–Q(7) and Q(11) lines of the d−a (0,0) band, while the SiH* emission intensities were obtained (with lower spatial resolution) by binning the $I_{em}(\lambda, z)$ data into $\Delta z = 1.5$ mm wide strips and determining the SiH* contribution by PGOPHER simulation. The various emitters clearly display different spatial distributions. The $I_{em}(H_2^*)$ and $I_{em}(H^*)$ profiles are very similar to those reported in our previous studies of MW activated H_2 plasmas operating under the same conditions of p and P, peaking at $z \sim 2.5$ mm and $z \sim 7.5$ mm, respectively, and not extending beyond $z = 20$ mm.[54] The $^1Si^*$, $^3Si^*$ and SiH* emissions, in contrast, peak higher above the substrate (at $z \sim 10$ mm and $z \sim 12.5$ mm, respectively) and extend to $z > 27$ mm.

Varying $F(SiH_4/H_2)$: Figure 4 shows how the magnitudes and profiles of (a) $I_{em}(H_2^*)$, (b) $I_{em}(H^*)$, (c) $I_{em}(^3Si^*)$ and (d) $I_{em}(^1Si^*, 288\ nm)$ vary with $F(SiH_4/H_2)$. The $I_{em}(^1Si^*, 288\ nm)$ and $I_{em}(^1Si^*, 390\ nm)$ emissions show identical behaviour,[65] so the latter is not shown here. Figure 4(e) summarizes the $F(SiH_4/H_2)$ dependence of the summed intensities of these emitters and of $I_{em}(SiH^*)$ in limited spatial ranges ($9 \leq z \leq 12$ mm for $I_{em}(H^*)$, $I_{em}(^3Si^*)$, $I_{em}(^1Si^*)$ and $I_{em}(SiH^*)$, $0 \leq z \leq 3$ mm for $I_{em}(H_2^*)$). Each summed intensity plot is normalised to have a value of unity at base conditions (*i.e.* $F(SiH_4/H_2) = 15$ sccm). Figures 4(a), 4(b) and 4(e) demonstrate that $I_{em}(H_2^*)$ and $I_{em}(H^*)$ both decline quite steeply upon small additions of silane ($F(SiH_4/H_2) < 5$ sccm), but thereafter change little. In both cases, the decline is most marked at low z. $I_{em}(^3Si^*)$, $I_{em}(^1Si^*)$ and $I_{em}(SiH^*)$ all increase with increasing $F(SiH_4/H_2)$. The $I_{em}(^3Si^*, z)$ and $I_{em}(^1Si^*, z)$ profiles at any given $F(SiH_4/H_2)$ are very similar at base p and P; both narrow with increasing $F(SiH_4/H_2)$ and their centres of gravity shift to lower z. The later analysis attributes the different $F(SiH_4/H_2)$ dependences of $I_{em}(^3Si^*)$ and $I_{em}(^1Si^*)$ at high $F(SiH_4/H_2)$ revealed in Figure 4(e) to self-absorption (of the triplet emission) in cooler regions of the reactor.

Varying Pressure, p: The presence of $F(SiH_4/H_2) = 15$ sccm causes no obvious changes to the previously reported [54] p-dependent $I_{em}(H_2^*, z)$ and $I_{em}(H^*, z)$ profiles measured in a pure H_2 plasma operating under otherwise the same conditions, and these data are thus confined to Figure S1 in the Supplementary Information (SI). These H_2^* and H^* emissions are induced by electron impact excitation (EIE) from within the high energy (hyperthermal) tail of the electron energy distribution function (EEDF). As in the case of the pure H_2 plasma,[54] $I(H_2^*)$ in the SiH_4/H_2 plasma initially increases, up to p ~75 Torr (reflecting the increasing H_2 density), but thereafter declines as a result of a combination of the increased excited state quenching rates and the decreasing hyperthermal component within the EEDF. $I(H^*)$ is also impacted adversely by the p-dependence of the high energy tail of the EEDF, but this is more than compensated by the greater than linear increase in the ground state H atom number density, [H], on account of the increase in T_{gas} (and thus in the thermal dissociation of H_2) in the hot plasma region as p is increased.[54]

Figures 5(a)–5(c) illustrate the distinctive p-dependences of $I_{em}(^3Si^*)$, $I_{em}(^1Si^*)$ and $I_{em}(SiH^*)$. As noted above, the $I_{em}(^3Si^*, z)$ and $I_{em}(^1Si^*, z)$ profiles are essentially identical at base conditions (recall Figures 4(c) and 4(d)), but they are clearly different at low pressures: $I_{em}(^3Si^*)$ at p ~50-60 Torr is relatively much more intense (*cf.* $I_{em}(^1Si^*)$) at small z. Figure 5(d) further illustrates how small increases in p cause large increases in both $I_{em}(^3Si^*)$ and $I_{em}(^1Si^*)$ at $p < 60$ Torr (though the exact magnitudes of the increases are observed to vary from one experiment to the next – possibly on account of the MW tuning and/or the condition of the inner walls of the reactor). All three emissions maximize at $p \sim 60$ Torr, under which conditions the peaks (z_m) of the $I_{em}(^3Si^*, z)$, $I_{em}(^1Si^*, z)$ and $I_{em}(SiH^*, z)$ profiles are at, respectively, $z_m \sim 9$, 10 and 12.5 mm. Another point of distinction is evident at high pressures: $I_{em}(^3Si^*)$ and $I_{em}(^1Si^*)$ both decline further upon raising p above 150 Torr, while $I_{em}(SiH^*)$ changes little.

Varying Power, *P*: The presence of $F(SiH_4/H_2)$ = 15 sccm also causes no obvious changes to the *P*-dependent $I_{em}(H_2^*, z)$ and $I_{em}(H^*, z)$ profiles measured in a pure H_2 plasma operating under otherwise the same conditions,[54] and these data are thus also confined to the SI (Figure S2). Both the peak and the radial extent of $I_{em}(H^*)$ increase roughly linearly with increasing *P*. The total $I_{em}(H_2^*)$ emission remains roughly constant but the peak of its profile shifts from $z_m \sim 7$ mm to $z_m \sim 2$ mm upon increasing *P* from 0.7 kW to 1.85 kW. As Figure 6 shows, $I_{em}(^3Si^*)$, $I_{em}(^1Si^*)$ and $I_{em}(SiH^*)$ respond similarly to increases in *P*. All three increase in the range $0.7 \leq P \leq 0.9$ kW, then decline in amplitude (but increase in spatial extent) upon further increases in *P*. These trends are summarized in Figure 6(d), which shows how the summed intensities of each of these three Si-containing emitters (and H*) vary with *P* in the spatial region $9 \leq z \leq 12$ mm. (For completeness, Figure 6(d) also shows the *P*-dependence of the summed H_2^* emission intensity in the range $0 \leq z \leq 3$ mm).

Using a Si wafer as the silicon source: As noted in section 2, additional experiments involving H_2 and H_2/Ar plasmas confirmed that a silicon wafer in good thermal contact with the Mo substrate can provide an alternative, less well-defined but nonetheless measurable source of gas phase SiH_x species. These gas-surface studies complement, but are distinct from, the main thrust of the present study. Representative data from these experiments are shown in Section 2 and Figure S3 in the SI and accompanied by discussion of the possible etching processes.

3.1.3 2-D Modelling of MW Activated Si/H Plasmas.

The Si/H kinetic data required to reveal and describe the main production and loss processes for the emitting species of current interest ($^1Si^*$, $^3Si^*$ and SiH^*) are derived by 2-D(*r*, *z*) plasma-chemical modelling, where *r* is the radial distance from the center of the top surface of the substrate (which defines $r = z = 0$). Such self-consistent modelling recently described for MW activated H_2,[54] H/Ar [66] and C/H [55] gas mixtures is here extended to the case of Si/H (and Si/C/H) plasmas. The specific blocks of the model address the plasma-chemical (~200 reactions involving 31 species for the Si/H plasma) and electron kinetics, heat and species transfer and gas-surface interactions, and solve Maxwell's equations to calculate the spatially dependent MW electromagnetic (EM) fields and MW power absorption in the Si/H plasma. The electron energy distribution functions (EEDFs) for all cells in the (*r*, *z*) grid are calculated from the Boltzmann equation and sets of e-H, e-H_2, e-SiH_x and e-ion collision cross-sections (for different gas mixture compositions, reduced electric fields and T_{gas}) to provide the necessary rate coefficients for the plasma-chemical and EM blocks.

The basic plasma-chemical kinetics mechanism involves the following charged species (electrons, H_x^+ (x = 1-3) and SiH_x^+ (x = 0-2) ions) and neutral species (H(n = 1-3) atoms, H_2 molecules in their ground ($X^1\Sigma_g^+$) and excited $B^1\Sigma_u^+$, $G^1\Sigma_g^+$, $a^3\Sigma_g^+$, $c^3\Pi_u$, $d^3\Pi_u$ and $e^3\Sigma_u^+$ states, Si atoms in the ground (^3P) state, in the $^1D_2$, $^1S_0$ and $^5S^o$ excited states (with respective excitation energies E = 0.78, 1.91 and 4.13 eV) and in the emitting singlet ($^1Si^*$) and triplet ($^3Si^*$) states derived from the $3s^23p^14s^1$ excited

configuration, SiH radicals in their ground $X^2\Pi$ and excited $A^2\Delta$ states (henceforth denoted as SiH and SiH*, respectively), $^1SiH_2$, $^3SiH_2$, SiH_3 and SiH_4. Expanded sets were also developed that additionally included the species H_xSiO (x = 0-2), SiO_2, O_2, O, OH, H_2O and H_3O^+ (to probe possible effects of oxygen in the gas mixture), Si_xH_y ($x \geq 2$) (to test for effects of silicon clustering and higher excited states of Si (Si** species with E > 6 eV in order to explore the effects of population cascade into the monitored ^{1}Si* and ^{3}Si* states). However, none of these extensions was found to have any significant influence under the process conditions of current interest (low oxygen contamination, and low silane mole fractions and high T_{gas} which both mitigate against silicon clustering [67]) and all results presented hereafter were obtained using the basic plasma-chemical mechanism. The core parts of this mechanism for the key species (SiH_x, Si($^1D_2$), ^{1}Si*, ^{3}Si*, SiH* and the various ions) are presented in Table 2. The reactions used for the Si($^1S_0$), Si($^5S^o$) and Si** species are not important in the context of this study and are omitted, while the kinetics for excited H* and H_2* species were as used previously.[54,55]

Insert Table 2 near here

Base conditions for the Si/H plasma modelling mimic those used in the experiments, *i.e.*, p = 150 Torr, P = 1.5 kW, a total gas flow rate of 315 sccm and a SiH_4 input mole fraction $X_0(SiH_4)$ = 48 ppm in H_2. The focus of the present work is the behavior of Si* and SiH* species and comparisons with the respective OE data measured as functions of p, P and $X_0(SiH_4)$. Based on our previous studies of C/H,[55,68] B/H [69] and B/C/H [70] plasma emissions, we can anticipate that the production and loss processes of the Si* and SiH* species will include electron impact excitation (EIE) from the respective lower lying (*i.e.* ground) states, radiative decay reactions, quenching processes (collisional and/or reactive quenching) and, possibly, additional sources like chemiluminescent (CL), dissociative EIE and electron-ion recombination reactions. Modelling these sources and sinks requires knowledge of the concentrations (and their spatial distributions) of the core neutral SiH_x (x = 0-4) and cationic SiH_x^+ species. The low (<1.5 eV) electron affinities of the SiH_x species makes it unlikely that there will be any significant concentrations of the respective negative ions.

There are additional reasons to study the SiH_x^+ ion chemistry. Addition of <120 ppm of silane has a visible effect on the H_2 plasma parameters, as can be seen from the changes in the I_{em}(H*) and I_{em}(H_2*) intensities and profiles (Figure 4). The present calculations show that addition of such low SiH_x fractions causes negligible perturbation of the EEDF of a pure H_2 plasma or the EIE rates of H and H_2. But SiH_x additives in an H_2 plasma do have at least two indirect influences on the plasma parameters. Electron impact ionization (EII) of SiH_x species constitutes an additional contribution to the total ionization, and changes the identity of the dominant ions which, in turn, affects the electron-ion recombination rates and the ambipolar diffusion coefficients. Thus, it is first necessary to explore the plasma-chemical kinetics of the neutral and cationic SiH_x species in order to develop the background necessary for any detailed consideration of the production and loss processes of the monitored ^{1}Si*, ^{3}Si* and SiH* species.

3.1.3.1 SiH_x Kinetics and Ion Conversion Reactions in a Hot MW-Activated Si/H Plasma.

SiH_x Kinetics and Electron Impact Ionization of SiH_x Species. As in previous simulations of the kinetics in C/H,[55] B/H [69] and N/H [71] gas mixtures, fast H-shifting reactions of the form $SiH_{x+1} + H \leftrightarrow SiH_x + H_2$ (reactions (1)-(6) in Table 2) ensure that the various SiH_x (x = 0-4) species in the hot plasma and nearby regions are in local equilibrium (*i.e*. that the rates of the forward and reverse reactions $R_i \approx R_{-i}$ are equal). Note that the SiH_2 species has a singlet ground state ($^1SiH_2$) and a low-lying triplet excited state ($\Delta E[^3SiH_2–^1SiH_2] = 0.91\pm0.03$ eV.[72] The present modelling assumes efficient state mixing between these two species and between the excited ($^1D_2$) and ground (^3P) states of atomic Si via reactions of the form $^3SiH_x + M \leftrightarrow {}^1SiH_x + M$ (where x = 0 and 2 and M = H and/or H_2). Various sets of rate coefficients (k_i) for these reactions are available in the literature.[51] We have probed various sets of k_i values and found no substantial differences in the calculated concentrations of SiH_x species (including $Si(^1D_2)$ atoms) or in their spatial distributions in the hot regions, with $R_i \approx R_{-i}$. This is unsurprising: the SiH_x concentrations in such equilibrium conditions are determined by thermochemistry,[73] the local T_{gas} and the $[H]/[H_2]$ ratio. As a result, the SiH_x species partition in favor of low ($x \leq 2$) species, mostly $Si(^3P)$ atoms. This is particularly so in the high gas temperature (T_{gas} ~3000 K) and H atom mole fraction (X_H ~0.1) values prevailing in the hot plasma region, but the H-shifting reactions (1)–(6) in Table 2 encourage conversion to SiH_x ($x \leq 1$) species throughout the entire reactor volume.

This partitioning is illustrated in Figure 7(a), which shows the calculated radial distributions of the SiH_x (x = 0-4) species concentrations at z =10.5 mm for base reactor conditions (r = 0, z = 10.5 mm corresponds to the center of the plasma core under base conditions). Figure 7(b) shows the corresponding radial distributions of T_{gas}, T_e, the H atom concentration, [H], and the electron and dominant ion concentrations at z = 10.5 mm for the same base reactor conditions. $Si(^3P)$ atoms dominate throughout the entire reactor volume: the predicted total $Si(^3P)$ content under base conditions (~4.5×10^{16} atoms) is two or more orders of magnitude higher than that of SiH_4 (~1.9×10^{14}), SiH_3 (~4.6×10^{11}), SiH_2 (~1.2×10^{13}), SiH (~9×10^{13}), $Si(^1D_2)$ atoms (~1.6×10^{13}) and all other silicon containing species. These data support the proposal that the different $F(SiH_4/H_2)$ dependences of $I_{em}(^3Si^*)$ and $I_{em}(^1Si^*)$ in Figure 4 are due to self-absorption of the former emission by the orders of magnitude greater ground (^3P) state number densities at large r ($[^3Si]$ ~4.7×10^{12} cm^{-3} in the hot core, *cf*. $[^3Si]$ ~ 2.4×10^{14} cm^{-3} near the reactor walls for base conditions). The predicted total contents in the higher lying $^1S_0$ and $^5S^o$ states of Si are much lower still (~2.7×10^{10} and ~2.4×10^9 atoms, respectively) and have negligible effect on the SiH_x species distributions or the distributions of the emitting species of current interest.

As Figure 7 also shows, the calculated Si concentrations in the plasma core are, respectively, 4 and 5 orders of magnitude lower than the concentrations of H atoms and H_2 molecules, respectively. Nonetheless, EII of $Si(^3P)$ and $Si(^1D_2)$ atoms (with respective EII cross-sections from ref. 74) and of SiH radicals [75] (reactions (7)-(9)) contributes ~25% of the total EII rate – due to their low ionization

potentials: IP_{SiH} = 7.9 eV and $IP_{Si(3P)}$ = 8.15 eV, *cf.* IP_H = 13.6 eV and IP_{H2} = 15.4 eV. But we also note that EII (of H_2, H and the various SiH_x species) only contributes ~30% of the total ion yield; most ions are formed via associative ionization (AI) reactions, particularly $H^* + H_2 \rightarrow H_3^+ + e$.[54] The present 2-D modelling shows that the rates of possible associative ionization reactions involving Si containing species (*e.g.* $Si^* + H \rightarrow SiH^+ + e$) are not competitive with the hydrogen-based AI sources.

Ion Conversion Reactions and the Effects of SiH_x^+ Ions. The dominance of Si atoms also directly impacts on the interconversion between ions when SiH_4 is added to an established H_2 plasma. Specifically, the dominant ions change from H_3^+ (ref. 54) to SiH_x^+ as a result of the charge-exchange reactions (10)-(12).[76] The exothermic reactions (10) and (11) favor SiH_x^+ ions, as expected given the low ionization potentials of the corresponding neutrals: $IP_{Si(3P)}$ = 8.15 eV, IP_{SiH} = 7.9 eV, IP_{SiH2} ~9 eV. The effect of the $H_3^+ \rightarrow SiH_x^+$ conversion is clear to see in Figure 7(b). The prevalence of Si^+ ions is determined by the balance of the fast forward (12) and reverse (–12) reactions: $[Si^+]/[SiH^+] \sim k_{12}[H]/(k_{-12}[H_2]) > 1.7$ for the present conditions. The thermal decomposition and reverse association reactions $SiH_x^+ + M \leftrightarrow SiH_{x-1}^+ + H + M$ (where M is a third body) for x = 1 and, particularly, x = 2 are less important than reactions (12) and (–12) under the conditions prevailing in the hot plasma region, ensuring that $[SiH_2^+] << [Si^+]$. The recombination rates of Si^+ ions with electrons (photo-recombination and/or three-body recombination) are very low compared with the dissociative recombination reactions (13),[77] (14), (20) and (27) [78] under the conditions of current interest. Note that the present analysis has assumed a 2-fold reduction in the tabulated [77] rate coefficient for reaction (12) at high T_{gas} (~3000 K). The (unknown) partitioning of the products of the $SiH^+ + e$ recombination reaction is discussed below (Section 3.2.2.2).

Three effects – the additional ion source from EII of Si atoms, the absence of any effective gas-phase loss process for the dominant Si^+ ion and the lower ambipolar diffusion coefficients of SiH_x^+ (*cf.* H_3^+) ions – all act to decrease the averaged reduced electric field (and thus T_e and the hot tail of the EEDF) upon small additions of SiH_4 to an H_2 plasma. Lower EM fields are needed to maintain the same electron concentration required for absorption of the given MW power when the source of ions is increased and the gas-phase and surface losses of the charged species are reduced. These effects will be partially compensated by the increased $SiH^+ + e$ dissociative recombination rate (*cf.* the rate of the $H_3^+ + e$ recombination reaction (13)) upon gradually transitioning from H_3^+ to SiH_x^+ as the SiH_4 fraction is increased. The 2-D modelling, which includes all processes shown in Table 2 with rate coefficients defined for the conditions of interest, generally reproduces the observed changes in the profiles of, and the decreases in, $I_{em}(H^*)$ and $I_{em}(H_2^*)$ upon adding SiH_4 (shown in Figure 4) and their variations with p and P (Figures 5 and 6, respectively) as shown in Figures S4-S6 in the SI. The model predictions still deviate from experimental observation in three details, however. The modelling does not reproduce the 'saturation' of the observed $I_{em}(H^*)$ and $I_{em}(H_2^*)$ depletions once $X_0(SiH_4) \geq 30$ ppm (*i.e.* $F(SiH_4/H_2)$

≥ 10 sccm, Figure 4), nor the observed *P*-dependent increase in $I_{em}(H_2^*)$ (Figure 6(d)), nor does it capture the low *z* peak in the $I_{em}(H_2^*)$ distributions observed, and discussed, in earlier studies of MW-activated H_2 plasmas.[54] Such discrepancies are not surprising, given the complex balances between the proposed processes (for which rate coefficients are not well known, especially for the prevailing hot plasma conditions).

As an aside, we recognize that similar processes may be responsible for the previously reported decreases in H* and H_2* emission intensities upon adding B_2H_6 to an H_2 plasma.[69] The degree of B_2H_6 decomposition is much lower (*cf.* SiH_4), so the total content of B_2H_6 molecules in the reactor will be much higher than the sum of all BH_x (x = 0-3) species. We start by considering the situation where the concentration of any air impurity is much lower than that of the added diborane, *i.e.* $2\times X_0(B_2H_6) >> X_{air}$). The H-shifting reactions in this case do not drive the BH_x family so strongly in favor of B atoms ([B] ~ ([BH] + [BH_3]) in the hot plasma region), but the presence of BH_x species with low ionization potentials and of BH_x^+ ions with increased BH_x^+ + e dissociative recombination rates will induce qualitatively similar effects to those discussed above for a dilute Si/H plasma. For completeness, we note that our earlier B/H plasma studies [69] actually involved a significant level of air contamination (X_{air} ~ $2\times X_0(B_2H_6)$), under which conditions the most abundant additives to the plasma core are likely to have been H_2O and HBO species, which will support formation of other ions (H_3O^+, H_xBO^+) by charge exchange and/or EII.

We now return to consider the present Si/H plasma with negligible air contamination. Having established concentration distributions of the key SiH_x neutrals and SiH_x^+ ions, we can now develop and probe production/loss mechanisms for the emitting species (^{1}Si*, ^{3}Si*, SiH*) monitored in the OE imaging studies.

3.1.3.2. Kinetics, Spatial Profiles and Process Parameter Dependences of ^{1}Si*, ^{3}Si* and SiH*.

As in the recent analysis of OE from different excited states of the CH radical in MW-activated C/H plasmas,[55] the modelling of the ^{1}Si*, ^{3}Si*, SiH* species started with the simplest production and loss scheme, namely, electron impact excitation (EIE) from the respective ground states (Si(^{3}P) and SiH) and radiative decay. The results returned by the 2-D model assuming such a simple kinetic scheme were far from the OE data, however, both in terms of the spatial profiles and the observed *p*- and *P*-dependences of the emission intensities. Guided by the analysis of CH* emissions from C/H plasmas,[55] we then investigated the possible effects of additional processes that could affect the SiH* and Si* populations (and their emissions), *i.e.* chemiluminescent (CL) sources, electron-ion recombination reactions, state mixing reactions, quenching processes, *etc*. Systematic calculations (involving thousands of 2-D model runs) with various reaction mechanisms were undertaken to establish the more important processes and the relevant kinetics. A summary description of these searches now follows, starting with the simpler SiH* kinetics.

SiH* Production and Loss Processes. Preliminary analysis and rate estimates encouraged omission of the following processes because of their minor importance under the prevailing conditions: (i) dissociative EIE reactions of the form $SiH_{x+1} + e \rightarrow SiH_x^* + H + e$ (x = 0, 1), due to their high threshold energies and the relative SiH_x populations ([SiH_2] << [SiH] << [Si]), and (ii) the dissociative electron-ion recombination $SiH_2^+ + e \rightarrow SiH^* + H$, the possible contribution from which would be uncompetitive relative to that from direct EIE of SiH. Supplementing this simplest mechanism (*i.e.* reactions (15) and (16) in Table 2) with an additional source and loss term (the chemiluminescent $Si(^1D_2) + H_2 \leftrightarrow SiH^* + H$ reaction (17) and the reactive quenching reaction (–17) in Table 2), however, enables reasonable agreement between the calculated column densities {SiH*}(z) – in terms of their spatial profiles and their dependences on $X_0(SiH_4)$, p and P (Figures 8(a), 8(b) and 8(c)) – and the corresponding I_{em}(SiH*) intensities (first shown in Figures 4-6). The (r = 0, z) rate profiles of these four processes are shown in Figure 9 for p = 60, 150 and 250 Torr, with all other parameters fixed at their base values. At high pressures ($p \geq$ 150 Torr), comparably good matches with the experimental data can be obtained assuming alternative CL sources (with the reversible reactions (17a) or (17b) and the parameters listed in Table 2). However, these alternative sources substantially underestimate {SiH*}(z) at low pressures (*e.g.* by a factor of ~2.3 compared with the p = 60 Torr {SiH*}(z) values shown in Figure 8(b)) and return a SiH*}(z) profile that is shifted further from the substrate (and thus further from the experimental observation). Figure 9 also allows us to assess the obvious inconsistencies (*cf.* experiment) in the {SiH*}(z) profiles and their p-dependence if the local balance is assumed to depend on just EIE (reaction (15)) and radiative decay (reaction (16)) rather than the four processes (15), (16), (17) and (–17).

Several previous studies have used analyses of wavelength resolved SiH* emission from other (generally cooler) Si/H plasmas to estimate gas temperatures.[79-83] The best-fit rotational temperature for the SiH* emission spectrum recorded under the present base conditions (T_{rot} ~2450±200 K) is lower than the gas temperature calculated from the 2-D model outputs using the expression $\langle T_{gas} \rangle = \int T_{gas}(r, z)[\text{SiH*(v=0)}](r, z)dr / \int [\text{SiH*(v=0)}](r, z)dr$ ~ 2935 K at z = 10.5 mm. The SiH* rotational state population distribution in the present study could be out of local thermodynamic equilibrium (*i.e.* $T_{rot} < T_{gas}$) if the rates of rotational-translational (RT) relaxation of the SiH* species, *i.e.* SiH*(v, N+ΔN) + M ↔ SiH*(v, N) + M are comparable with the SiH* production rate via the endothermic CL reactions (17). We have no data relating to the rate coefficients $k_{RT}(H_2)$ and k_{RT}(H) for RT relaxation of SiH* with the main collision species H_2 and H, but the 2-D modeling suggests that the relation $T_{rot} < T_{gas}$ could be achieved under the present plasma conditions if $k_{RT}(H_2)$ and k_{RT}(H) are not much greater than 5×10^{-11} and 5×10^{-10} cm^3 s^{-1}, respectively.

^{1}Si* and ^{3}Si* Production and Loss Processes. Excited state Si* atoms might be expected to be extremely reactive in a hot H_2 plasma. The kinetics of Si* species are complicated by the diversity of potentially important pathways, *e.g.* state mixing reactions $^1Si^* + M \leftrightarrow {}^3Si^* + M$, reactive quenching

via collisions with H_2 molecules, associative ionization (AI) in reactions with H atoms, different EIE probabilities from different lower levels (*i.e*. from ground triplet *cf*. metastable singlet states) and cascades from a range of upper states, *etc*. We have probed many possible reactions and their effects on the $\{Si^*\}(z)$ profiles and their *p*- and *P*-dependences. In addition to the traditional EIE sources (reactions (18), (19) and (26)) and radiative loss processes (reactions (24), (25) and (30)), the mechanism reported in Table 2 includes additional important Si* source and loss terms – the dissociative recombination reactions (20) and (27) and reactive quenching on H_2, reactions (22) and (28), respectively. The rate coefficients $k_i(T_e)$ for all electron induced reactions (apart from those with unknown cross-sections), with respective energetic thresholds E_{thr}, were calculated from the respective high energy 'tail' of the EEDF (with $E > E_{thr}$) and approximated as functions of T_e in Table 2 for presentation purposes only (and are applicable only over the limited range $0.9 < T_e < 1.7$ eV). These additional processes, together with EIE and radiative decay and the state mixing reactions (21) and (−21), determine the $^1Si^*$ column density profiles $\{^1Si^*\}(z)$ and their variations with changes in process conditions. As Figure 10 shows, these agree well with the observed variations in $I_{em}(^1Si^*)$ – with the greatest discrepancies evident at low *p* and/or *P*. This comparison is considered to be most appropriate, as the OES measurements sample the full depth of the plasma. The corresponding $\{^3Si^*\}(z)$ profiles are shown in Figure S7, and the calculated rate profiles $R_i(r = 0, z)$ for these various processes for $^1Si^*$ and $^3Si^*$ at $p = 60$, 150 and 250 Torr are shown in Figures S8 and S9, respectively. Inspection of these figures shows that EIE processes are relatively more important for $^3Si^*$ species, especially at low pressures – consistent with the observation (Figure 5) that $I_{em}(^3Si^*)$ peaks nearer the substrate than $I_{em}(^1Si^*)$, *i.e*. at lower *z*, where the EIE rates are maximal (Figures S8 and S9).

The 2-D model shows the $^3Si^*$ concentration in the hot emitting region increasing almost linearly with $F(SiH_4)$ – reflecting the linear increases in both $[Si(^3P)]$ and the main source (the EIE rate) of $^3Si^*$ under conditions of broadly constant n_e and T_e. As noted above, the observed saturation of $I_{em}(^3Si^*)$ is attributable to reabsorption of this emission by the column of $Si(^3P)$ atoms. The $^1Si^*$ emissions at 390 and 288 nm, in contrast, should not be affected by such reabsorption since, as Figure 7(a) shows, the respective lower state concentrations are much lower ($[Si(^1S_0)] << [Si(^1D_2)] << [Si(^3P)]$). Yet, both the measured $I_{em}(^1Si^*)$ intensities (Figure 4e) and the calculated $\{^1Si^*\}$ column densities appear to start levelling off at high $F(SiH_4)$. The 2-D modelling reveals that this trend is due to saturation of $[SiH^+]$ and thus of the main source of $^1Si^*$ (the $SiH^+ + e$ dissociative recombination reaction); at high $F(SiH_4)$, the efficiency of the $H_3^+ \rightarrow SiH_x^+$ ion conversion reaction ensures $[H_3^+] << [SiH_x^+]$ and that any further increases in $F(SiH_4)$ have progressively less effect on $[SiH^+]$.

Effects of Silicon Deposition and Etching Processes on Si Content and Plasma Emission. At the outset, we note that the elemental Si/H ratio in the source gas mixture (*e.g*. $\sim 2.4\times10^{-5}$ for a 48 ppm SiH_4/H_2 mixture) does not ensure the same Si/H partitioning throughout the entire reactor volume. As with dilute CH_4/H_2 plasmas,[10] the Si content in the hot plasma core is reduced substantially (more than

3-fold) by thermodiffusional transfer (the Soret effect) and, to a lesser degree, by H_2 dissociation (the maximal H atom mole fraction, $X(H) > 0.1$). Further, the total silicon content in the whole reactor volume will be sensitive to any silicon deposition and/or etching processes at the reactor walls. Serial experimental investigations of many Si/H plasmas result in a visible deposit on the inner walls of the reactor. This is not surprising, given the high Si atom concentrations predicted at the outer extremities of the reactor (*e.g.* [Si](r = 60.5 mm, z) ~2.4×10^{14} cm^{-3}, Figure 7(a)) for the current base conditions. The near-wall Si and H atom concentrations (*i.e.* [H](r = 60.5 mm, z) ~ 10^{12}-10^{13} cm^{-3} for base conditions, Figure 7(b)) vary with location and with process conditions (*i.e.* p, P and $X_0(SiH_4)$), resulting in different rates of Si deposition and, quite possibly, H atom etching of any Si deposit. Under steady state conditions (if these are reached), an appropriate near-wall Si concentration (and thus a total silicon content in the reactor volume) is established, wherein the supply of silicon from the SiH_4/H_2 gas source and any etching are balanced by silicon deposition on the walls and by the evacuation of gas from the reactor volume.

Such Si deposition/etching processes are likely to have a significant impact on the total silicon content, as illustrated by additional 2-D model calculations that assume a (hypothetical) Si net deposition probability, $\gamma_{Si} = 0.001$. The actual Si deposition probability and the probability of etching (by H atoms), g_{etch}, under the present conditions are unknown. But we note the following. First, even this small chosen γ_{Si} value (which is more than two orders of magnitude smaller than the adsorption probability assumed for the SiH_3 precursor in Si deposition models ($\gamma_{SiH3} = 0.25$) [84]) provides an integral Si loss rate comparable to the SiH_4 supply under our base conditions. Second, silicon etching from the reactor side walls under the present experimental conditions (*i.e.* near-wall H atom concentrations, $[H]_{wall}$ ~10^{13} cm^{-3} and a total side wall area S_{wall} ~200 cm^2) provides an SiH_x source ~ $g_{etch} \times 1.2\times10^{20}$ s^{-1} which would be equivalent to the base SiH_4 supply (*i.e.* 0.015 sccm of SiH4) even when assuming a g_{etch} ~10^{-4}. Measured etch rates for amorphous silicon in a hot filament (HF) CVD reactor [85] hint at significantly higher g_{etch} values. Any imbalance in the deposition/etching rates (caused, for example, by changing process parameters) will thus affect the total silicon content and trigger an appropriate restoration of this balance. The OE data for Si/C/H plasmas described in section 3.2 provide (indirect) evidence for the existence and violation of this balance between Si deposition and etching processes.

Summary. The foregoing discussion provides a reasonably complete and consistent rationale for the observed H*, H_2*, ^{1}Si*, ^{3}Si* and SiH* emissions from MW-activated dilute Si/H plasmas operating at gas temperatures and pressures such as are used in diamond CVD, and their variations with process conditions. Key features of the analysis include (i) the fast H-shifting reactions ensure that Si atoms are the dominant Si-containing species throughout the whole reactor volume, (ii) the low ionization potentials of all SiH_x (x = 0-4) species and the ion conversion reactions (10)-(12) ensure that even trace (<50 ppm) additions of silane to an H_2 plasma are sufficient to change the dominant ions (from H_3^+ to SiH_x^+), with knock-on consequences for electron-ion recombination rates and ambipolar diffusion

coefficients, (iii) the spatial profiles of the ^{1}Si*, ^{3}Si* and SiH* emissions and their variations with process conditions require recognition that, for all three species, CL reactions supplement EIE as sources of excited state species and that both radiative decay and reactive quenching contribute to the loss of these species, and (iv) the total content of silicon species in the reactor volume can be affected by silicon deposition and etching processes on the reactor walls.

3.2 Si/C/H Plasmas

3.2.1. Optical Emission Images and Their Analysis

Upon adding CH_4, the characteristic H*, H_2*, ^{1}Si*, ^{3}Si* and SiH* emissions from the Si/H plasma are supplemented by CH* and C_2* emission bands. This range of species, combined with the high T_{gas} values, results in rich spectra – as illustrated by the spatially-resolved false colour $I_{em}(\lambda, z)$ images of the emissions from a Si/C/H plasma operating under base conditions (*i.e.* $F(H_2)$ = 270 sccm, $F(CH_4)$ = 19 sccm, $F(SiH_4/H_2)$ = 30 sccm, corresponding to $X_0(SiH_4)$ = 94 ppm, p = 150 Torr and P = 1.5 kW) shown in Figure S10. This Figure presents data for the wavelength ranges (a) $372 \leq \lambda \leq 447$ nm and (b) $463 \leq \lambda \leq 534$ nm and the corresponding $I_{em}(\lambda)$ plots obtained by summing all emission intensity in the range $10.5 \leq z \leq 12$ mm for the wavelength ranges (c) $386 \leq \lambda \leq 435$ nm and (d) $496 \leq \lambda \leq 519$ nm. The ^{3}Si* features, which appear in second order, are largely buried by the much more intense $C_2(d \rightarrow a)$ Swan band emission (appearing in first order) but can be observed cleanly by placing a suitable narrow-band UV transmission filter in the optical path between the reactor and the spectrometer entrance slit.

Figures 11 and 12 illustrate how these emissions vary upon adding, respectively, CH_4 to a pre-existing Si/H plasma and SiH_4 to a pre-existing C/H plasma operating under the base conditions defined in Section 2. As Figure 11 shows, $I_{em}(H_2$*) and I_{em}(H*) both increase ~2-fold upon adding as little as $F(CH_4)$ = 1 sccm to the Si/H plasma but are relatively invariant to further increases in $F(CH_4)$, while $I_{em}(C_2$*) and I_{em}(CH*) scale as ~$F(CH_4)$ and ~$F(CH_4)^{0.5}$, respectively. These trends, and the dependencies of these various emission profiles on changes in p and P, mimic those reported previously when adding CH_4 to a pre-existing hydrogen plasma. The increases in $I_{em}(H_2$*) and I_{em}(H*) reflect the change in dominant ion (from H_3^+ to $C_2H_2^+$ and $C_2H_3^+$ in the C/H plasma) and the consequent changes in the electron characteristics, T_{gas} and the absorbed power densities.[7,10] The $I_{em}(C_2$*) ~ $F(CH_4)$ and I_{em}(CH*) ~ $F(CH_4)^{0.5}$ trends follow from documented differences in the thermal chemistry that underpins the formation and equilibration of these two species.[10] Thus, notwithstanding the high cross-sections for forming SiH_x^+ ions (with x = 0 and 1) in the pre-existing Si/H plasma, the data in Figure 11 imply that introducing as little as $F(CH_4)$ = 1 sccm is sufficient to enhance the hot 'tail' of the EEDF (*i.e.* the part of the EEDF responsible for EIE of the H* and H_2* species) as a result of converting some SiH_x^+ ions into C-containing ions (analogous to the conversion of H_3^+ to C-containing ions when transitioning from an H_2 to a C/H plasma [10]).

This conclusion is reinforced by the data shown in Figure 12. Progressive addition of SiH_4 to a pre-existing C/H plasma operating under base conditions causes no discernible change to the $I_{em}(H_2^*)$, $I_{em}(H^*)$, $I_{em}(C_2^*)$ or $I_{em}(CH^*)$ intensities or profiles. This is unsurprising, given that the SiH_4 fraction in the Si/C/H input gas mixture under base conditions ($X_0(SiH_4)$ = 94 ppm) is already 32-times less than the carbon fraction when $F(CH_4)$ = 1 sccm; this Si/C ratio decreases to less than 1 in 500 for a plasma operating with $F(CH_4)$ = 19 sccm. As Figure 12(c) shows, $I_{em}(^3Si^*)$, $I_{em}(^1Si^*)$ and $I_{em}(SiH^*)$ all increase near-linearly with increasing $F(SiH_4/H_2)$. The observed monotonic increase in $I_{em}(^3Si^*)$ across the full $F(SiH_4/H_2)$ range – essentially replicating the $F(SiH_4)$-dependence of $I_{em}(^1Si^*)$ – is noteworthy and contrasts with that seen with the C-free Si/H plasma (recall Figure 4(e)).

The changes in $I_{em}(^3Si^*)$, $I_{em}(^1Si^*)$ and $I_{em}(SiH^*)$ upon adding CH_4 to the pre-existing Si/H plasma are more dramatic. Figures 13(a) and 13(b) show $I_{em}(^3Si^*)$ and $I_{em}(^1Si^*, 288\ nm)$ profiles upon introducing progressively larger $F(CH_4)$ to the base Si/H plasma. As Figure 13(c) shows, the $I_{em}(SiH^*)$ profile maximizes at, and extends to, larger z than either $I_{em}(Si^*)$ profile under base conditions. Such trends were observed for the CH_4-free plasma also (recall Figure 3), but the $I_{em}(^3Si^*)$ and $I_{em}(^1Si^*, 288\ nm)$ profiles in the presence of $F(CH_4)$ = 19 sccm under base conditions are clearly less extensive (*cf*. Figure 5). Figure 13(d) shows that all three emissions and, particularly, $I_{em}(^1Si^*)$ and $I_{em}(SiH^*)$ decline steeply upon introducing small amounts of CH_4 to the Si/H plasma, but are then relatively insensitive to further increases in $F(CH_4)$.

3.2.2 2-D Modelling of MW Activated Si/C/H Plasmas.

A full 2-D model involving the complete Si/C/H chemistry is impractical given the paucity of information relating to many of the potentially important Si/C coupling reactions and their temperature dependences. Nonetheless, certain inferences and conclusions can be built from the present OE imaging measurements and approximate 2-D modeling of the Si/C/H plasma (56 species, 370 reactions) based on the previously established C/H plasma chemistry,[10,55] the Si/H plasma chemistry described in section 3.1, and a limited number of Si/C coupling reactions – specifically, additional ion chemistry enabling interconversion between SiH_x^+, $SiC_2H_y^+$ (y = 0-2) and $C_2H_y^+$ (y = 2,3) ions and SiH_x/C_2H_y couplings resulting in production of the SiC_2H_y (y = 0-2) species listed in Table 3.

Insert Table 3 near here

The 2-D modelling confirms that the apparent indistinguishability of the respective $I_{em}(H_2^*)$, $I_{em}(H^*)$, $I_{em}(C_2^*)$ and $I_{em}(CH^*)$ distributions from C/H and Si/C/H plasmas operating under base $F(CH_4)$, p and P conditions is indeed a reflection of the similar electronic (n_e, T_e, EEDF) characteristics of the two plasmas. But, as Figures 11 and 13 showed, adding $F(CH_4)$ = 1 sccm (*i.e*. just 0.33% CH_4) to a pre-existing Si/H plasma causes ~2-fold increases in $I_{em}(H^*)$ and $I_{em}(H_2^*)$ and very obvious decreases in $I_{em}(Si^*)$ and $I_{em}(SiH^*)$. The low hydrocarbon (and silicon) fractions in the dilute Si/C/H plasmas of current interest have minimal impact on the EEDF, which is largely determined by the various e-H_2 and

e-H collisions (rather than e-C_xH_y (or e-SiH_x) collisions). Indirect mechanisms by which CH_4 additions affect the EEDF (and cause the observed jumps in $I_{em}(H^*)$ and $I_{em}(H_2^*)$) are discussed below.

Ion Conversion Reactions. The former trends are successfully captured by the present 2-D modelling which shows that, as in the case of an H_2 plasma,[10] CH_4 addition to an Si/H plasma introduces an additional ionization source (EII of C_2H_2). This new ionization source has only limited effect on the plasma parameters at low (*i.e.* <0.33%) CH_4 fractions but has a substantial effect on the ion partitioning and leads to increased electron-ion recombination rates. Specifically, the dominant ions in the Si/H plasma (*i.e.* SiH_x^+ and H_3^+ ions) are progressively converted to $C_2H_y^+$ and $SiC_2H_y^+$ ions via the fast forward and reverse reactions listed in Tables 2 (reactions (10)–(14)) and 3 (reactions (31)–(39)).[76] Any conversion of Si^+ ions (for which the photorecombination rate with electrons is extremely low, $\sim 4.4\times10^{-13}/T_e^{0.6}$, with T_e expressed in eV [ref. 76]) or of H_3^+ ions (for which the electron-ion recombination cross-section is also smaller than that for more complex ions [10]) into larger $C_2H_y^+$ and $SiC_2H_y^+$ ions boosts the overall loss of gas-phase charged species via dissociative electron-ion recombination reactions, which is compensated by increasing the power densities (and thus the EII rates) in the hot plasma region. The 2-D modeling reveals simultaneous changes to both the spatial distribution of the plasma (which shifts closer to the substrate) and the plasma parameters upon adding 0.33%CH_4; the maximal electron and H atom concentrations increase (by ~30% and ~50%, respectively) and the maximal T_{gas} value increases by ~3% (by ~85 K). Such plasma modifications are wholly consistent with the observed (Figure 11) increases in $I_{em}(H^*)$ and $I_{em}(H_2^*)$ upon adding $F(CH_4)$ = 1 sccm to a 94 ppm Si in H_2 plasma operating under base conditions of p and P.

The main ion conversion reactions in an Si/C/H plasma operating under conditions of present interest are presented in Table 3. The 2-D model identifies Si^+ as the most abundant Si-containing ion in the hot plasma core, with a concentration ($\sim1.5\times10^{11}$ cm^{-3} at r = 0, z = 10.5 mm) comparable to that of $C_2H_3^+$. $[SiH^+]$ is predicted to be $\sim[Si^+]/2.5$. $[H_3^+]$, $[C_2H_2^+]$ and $[SiC_2H^+]$ are all predicted to be an order of magnitude smaller than $[Si^+]$ – as detailed in the caption of Table 3 – and the predicted concentrations of all other ions are $<2\times10^7$ cm^{-3}.

The 2-D Si/C/H model also predicts that {H*} and {H_2*} saturate upon further increases in $F(CH_4)$, consistent with the observed trends in $I_{em}(H^*)$ and $I_{em}(H_2^*)$ (Figure 12). Once $F(CH_4) \geq 1$ sccm, the C_2H_2 concentration (and the contributions from EII of C_2H_2) increases linearly with $F(CH_4)$ and the pre-existing SiH_x^+ (x = 0, 1) ions are progressively replaced by $C_2H_y^+$ and SiC_2H^+ ions (predominantly $C_2H_3^+$ ions). The 2-D modeling suggests that the increased recombination losses of these polyatomic charged species are largely compensated by an increase in the EII of C_2H_2. (EII of C_2H_2 is calculated to be the dominant EII source at $F(CH_4)$ = 9 sccm (3%CH_4)), at which point EII becomes comparable to the main associative ionization sources (*i.e.* sources $H(n \geq 2) + H_2 \rightarrow H_3^+ + e$). As a result, the basic plasma

parameters (T_e, T_{gas}, n_e, EEDF) are predicted to vary little once $F(CH_4)$ >1 sccm, consistent with the observed near-constancy of the $I_{em}(H^*)$ and $I_{em}(H_2^*)$ signals at higher $F(CH_4)$ (Figure 12(c)).

Si/C Coupling Reactions. The explanation for the marked declines in $I_{em}(Si^*)$ and $I_{em}(SiH^*)$ upon introducing $F(CH_4)$ = 1 sccm to a dilute Si/H plasma operating under base conditions of p and P (Figure 13) is less straightforward and implies some coupling between the Si/H and C/H chemistries and/or indirect coupling effects. C_2H_2 is the dominant C-containing species in the hot regions of the C/H plasma, and previous gas kinetic studies have determined that Si atoms in both their ground (^3P) and metastable excited (^1D) states react with C_2H_2 at room temperature at near gas kinetic collision rates.[86-88] Experiment and theory suggest that Si(^3P) addition of C_2H_2 is a barrierless process, wherein the atom interacts with the π-system of the C_2H_2 to form a cyclic c-SiC_2H_2 intermediate. The fate of this adduct remains a subject of debate. H_2 elimination, yielding c-SiC_2 as the co-product, following intersystem crossing to a lower lying triplet state has been proposed to account for the high removal rates measured at low temperatures (*e.g.* $T_{gas} \leq 300$ K),[89,90] as has collisional stabilization [91,92] and, at higher collision energies (*e.g.* ~0.16-0.55 eV in crossed beam experiments), rapid re-dissociation.[93] The collisional stabilization route would require extremely high rate coefficients ($>10^{-27}$ cm^6 s^{-1}) in order to accommodate the measured reaction rates in terms of the three-body process Si(^3P) + C_2H_2 + M → c-SiC_2H_2 + M.[89] Kaiser and Gu determined an endothermicity $\Delta_r H$ ~0.87 eV for the bimolecular reaction Si + C_2H_2 ↔ Si–C≡CH + H,[93] and we assume this reaction to be important under the present conditions and adopt it (reaction (−40)) and the reverse reaction (40) in Table 3 in the current modeling. The unknown rate coefficient k_{40} for the exothermic reaction (40) was assumed to be temperature independent and k_{-40} was calculated from thermochemical data for the given k_{40}. These reactions are in equilibrium in the hot plasma region, and varying k_{40} in the range ~10^{-11}–10^{-10} cm^3 s^{-1} has little impact on the overall modelling. Some c-SiC_2H_2 species will likely isomerize (*e.g.* the acyclic H_2CCSi and HCCSiH isomers are both only ~75 kJ mol^{-1} higher in energy) [92] and all will undergo H-shifting reactions of the form SiC_2H_2 +H ↔ SiC_2H + H_2. The acyclic SiC_2H species is calculated to be ~25 kJ mol^{-1} more stable than c-SiC_2H. The final step SiC_2H + H ↔ SiC_2 + H_2 is exothermic and presumed to be fast, so could constitute another potential route to SiC_2 species in the hotter regions.

A combination of crossed molecular beam studies and *ab initio* electronic structure calculations have also demonstrated barrierless formation of the c-SiC_2H_2 intermediate (together with an H atom) in SiH + C_2H_2 collisions.[94] CH_4 will be the dominant hydrocarbon in the cooler peripheral regions of a MW reactor operating with a CH_4/H_2 input gas mixture. The reported rate constant for the Si(^3P) + CH_4 reaction at 300 K is $<10^{-14}$ cm^3 s^{-1} (ref. 86), consistent with the endothermicity (~147 kJ mol^{-1}) for forming SiH + CH_3 products. The near gas kinetic rate constant measured for removal of Si(^1D) atoms in collisions with CH_4 at 300 K [87] is attributed to efficient quenching rather than reaction.

Various gas phase Si/C coupling schemes (of which reactions (40)–(46) in Table 3 are the most important) were included in the present 2-D modelling but none caused a significant reduction in the predicted {Si*} and {SiH*} column densities (such as could explain the observed decrease in I_{em}(Si*) and I_{em}(SiH*) upon introducing $F(CH_4)$), nor challenged the dominance of Si atoms in the hot plasma center, where the concentrations returned by the modeling for a 0.01%SiH_4/0.33%CH_4/H_2 mixture operating at base p and P are: [Si] ~9×10^{12} cm^{-3}, [SiH] ~8×10^{11} cm^{-3} and [SiC_2] ~6.4×10^{10} cm^{-3}. The relative concentration of SiC_2 (which is predicted to be the most populated species within the SiC_2H_y family) increases in the cooler regions. Close above the substrate, [SiC_2] is predicted to be ~5.5×10^{12} cm^{-3} (*cf.* [Si] ~4.2×10^{13} cm^{-3}) with this Si/C/H input gas mixture, and to increase progressively with increasing $F(CH_4)$ such that [SiC_2] is predicted to exceed [Si] in the cool near wall and near substrate regions at higher $F(CH_4)$; *e.g.* [SiC_2] ~2.6×10^{13} cm^{-3}, *cf.* [Si] ~2×10^{13} cm^{-3} above the substrate center for a 0.01%SiH_4/3%CH_4/H_2 gas mixture.

It is important to note that the rates of the forward and reverse H-shifting reactions in the SiH_x family (reactions (1)-(6) in Table 2) and in the SiC_2H_y family (reactions (45)-(46) in Table 3) are close to equilibrium, especially in the hot plasma region. Thus the relative population distributions within each family are largely determined by the thermochemical properties of the species,[73,95] the local T_{gas} and the [H]/[H_2] ratio, and are rather insensitive to the choice of the (unknown) reaction rate coefficients. Similar facile interconversions and stable partitioning is anticipated within the SiH_x^+ and $SiC_2H_y^+$ ion families and within the $SiCH_x$ family, wherein the fast Si + CH_3 ↔ $SiCH_2$ + H reaction (k ~10^{-9} cm^3 s^{-1} (ref. 76)) and the thermochemical properties of the various $SiCH_x$ species suggest that $SiCH_2$ is probably the most stable $SiCH_x$ species.

Gas-Surface Interactions. The deduced stability of the gas phase interconversions leaves no possibility of explaining the observed drop in I_{em}(Si*) and I_{em}(SiH*) upon adding CH_4 simply in terms of gas-phase chemistry. However, the present 2-D modelling allows us to propose an alternative, less direct but potentially important effect based on the global balance of silicon deposition and etching processes. Namely, CH_4 addition to a Si/H (or a pure H_2) plasma causes a significant drop in the H atom concentrations in the cooler regions, where H atoms are consumed in a variety of gas-phase hydrocarbon conversion reactions.[7,8,10,96]

The maximal $[H]_{wall}$ values near the reactor wall (*e.g.* at $r = R_{reac}$ = 61 mm, z ~ 22 mm) are predicted to drop by orders of magnitude upon adding CH_4 to a pre-existing 0.01%SiH_4/H_2 plasma operating under base p and P. Illustrative values from the present 2-D modelling are $[H]_{wall}$ ~4×10^{13} cm^{-3}, ~1.7×10^{11} cm^{-3} and ~6×10^{8} cm^{-3} for gas mixtures containing, respectively, 0, 0.33% and 3%CH_4. The CH_4-induced reduction in $[H]_{wall}$ affects the balance of the H-shifting reactions also. This huge decline in $[H]_{wall}$ ensures that a much greater fraction of the input SiH_4 molecules survive in the cold regions when CH_4 is present (because the huge decrease in the rates of the various SiH_{x+1} + H ↔ SiH_x + H_2 reactions

(1) – (6)). For example, the predicted [SiH_4] at r ~61 mm, z ~22 mm in the absence of any CH_4 is only ~200 cm^{-3} whereas, upon introducing X_0(CH4) = 0.33% and 3%, [SiH_4] this increases to ~8×10^{13} and ~4.6×10^{14} cm^{-3}, respectively. The near-wall concentration of silicon atoms, $[Si]_{wall}$ (the most abundant SiH_x radical) is predicted to decline upon CH_4 addition – though much less dramatically than the decline in $[H]_{wall}$. Illustrative maximal $[Si]_{wall}$ values at r ~61 mm, z ~22 mm are ~4.5×10^{14} cm^{-3} and ~6.4×10^{13} cm^{-3} when 0.33% and 3%CH_4 (*cf.* $[Si]_{wall}$ ~6×10^{14} cm^{-3} for the CH_4-free Si/H plasma operating under otherwise identical conditions). [SiC_2H_y] and [$SiCH_x$] are predicted to increase with increasing $F(CH_4)$ and will also contribute to the overall Si/C deposition rate, but even when $X_0(CH_4)$ = 3%, the predicted sum of $[SiC_2H_y]_{wall}$ in the cooler near-wall regions is still only ~$[Si]_{wall}/3$. However, we also note that introducing a hypothetical Si + C_2H_2 ↔ SiC_2 + H_2 reaction (such as has been proposed previously to account for the measured loss rate of Si(^{3}P) atoms in collision with C_2H_2 at low temperatures,[89,90] and which thus might become relatively more important in the cooler, near-wall regions of the reactor) or the three-body reaction Si + C_2H_2 + M ↔ SiC_2H_2 + M could skew the near-wall partitioning in favor of SiC_2H_y species, such that [SiC_2H_y] >> [Si]. However, it is not obvious that changing the dominant Si-containing gas phase species (from Si to SiC_2) would necessarily impact on the overall silicon loss rate (by evacuation and/or by Si/C deposition).

The huge reduction in [H] near the reactor walls upon adding CH_4 to a pre-existing Si/H plasma will lead to a much-reduced etching rate of any Si already adsorbed on the reactor walls (*cf.* the etching rate in the C-free Si/H plasma that, under steady state conditions, would be required to compensate for the Si deposition rate). This will cause a net decrease in the global silicon content in the Si/C/H plasma (*cf.* the pre-existing Si/H plasma). Calculations comparing the Si supply (modelled as a gas flow, $F(SiH_4)$) and deposition rates suggest that introducing 0.33%CH_4 would cause the global Si content in the reactor to drop by amounts comparable to that seen in the I_{em}(Si*) and I_{em}(SiH*) measurements (Figure 13) if the Si incorporation probability, $\gamma > 10^{-2}$. As noted above, higher methane inputs (*i.e.* >0.33%CH_4) will cause a progressively greater decrease in $[Si]_{max}$ (and thus in the Si deposition rates). As a result, the global silicon content in the plasma (and the Si* and SiH* emission intensities) should stabilize – as observed (Figure 13) – at levels determined by the balance between the silicon supply ($F(SiH_4)$), the exhaust of the processed gas and deposition on the reactor walls.

The deduced decrease in [Si(^{3}P)] in the periphery of the reactor upon introducing CH_4 also provides an explanation for the differences in I_{em}(^{1}Si*) and I_{em}(^{3}Si*) observed upon adding $F(CH_4)$ = 1 sccm. The 2-D modelling suggests that CH_4 additions should impact Si*(^{3}P^o) and Si*(^{1}P^o) concentrations in the hot plasma region similarly. Yet, as Figure 13 showed, the observed decrease in I_{em}(^{1}Si*) on introducing $F(CH_4)$ = 1 sccm is ~5× greater than that of I_{em}(^{3}Si*). The smaller reduction in the case of I_{em}(^{3}Si*) can be traced to the reduced optical thickness of Si/C/H plasmas (*cf.* Si/H plasmas) at the Si*(^{3}P^o→^{3}P) resonance emission wavelengths (because of the CH_4-induced decrease in [Si(^{3}P)] in the cooler regions

of the reactor). That the $I_{em}(^1Si^*)$ and $I_{em}(^3Si^*)$ emissions show very similar $F(SiH_4)$-dependences in Si/C/H plasmas (Figure 12(c)) but obvious differences in Si/H plasmas (Figure 4(e)) can be similarly traced to the much reduced [Si(^{3}P)] in the periphery of the reactor and thus the reduced re-absorption of Si*($^3P^o \rightarrow {}^3P$) emission in the Si/C/H plasma.

Implications for CVD of Si-Doped Diamond. As noted at the start of Section 3.2, the paucity of data relating to potentially important Si/C coupling reactions and their temperature dependences preclude comprehensive 2-D modelling of the gas phase chemistry involved in the CVD of Si-doped diamond. Nonetheless it has been possible to develop a simplified model involving plausible Si/C coupling schemes for both ions and neutrals in the kinds of hydrogen-rich plasmas containing small (few %) concentrations of hydrocarbon and trace amounts of silicon that succeeds in replicating the limited experimental insights that can be gleaned by OE studies of MW-activated Si/C/H plasmas operating under conditions relevant for contemporary diamond CVD.

The experimental data (measurements of different species emissions as functions of process conditions) inform the 2-D modelling, which succeeds in revealing the main neutral SiC_2H_y and charged $SiC_2H_y^+$ species in the hot plasma region (SiC_2 and SiC_2H^+, respectively), their dominant production and loss mechanisms, and the extent to which adding CH_4 (SiH_4) to a pre-existing Si/H (C/H) plasma will affect the plasma parameters, the optical emissions and the deposition of Si and C on the substrate and the reactor walls. From the perspective of controllable Si-doped diamond CVD, the present study suggests that:

(i) the SiH_4/H_2 in the source gas should be introduced simultaneously with or shortly after establishing the C/H plasma (*i.e*. not before, to avoid poorly defined Si deposition on the reactor walls),

(ii) under these circumstances, changes in the ^{1}Si* and/or ^{3}Si* emission intensities should be reliable indicators of changes in the Si content in the hot plasma region,

(iii) a Si substrate or fused silica components within the reactor can easily constitute an (unintended) source of gas phase Si-containing species,

(iv) SiC_2 species and/or Si atoms will be the most abundant gas phase Si-containing species just above the growing diamond surface. Future theoretical studies of the possible gas-surface reactions will be required to establish how efficiently the Si in an incident SiC_2 species might be incorporated during diamond CVD.

4. CONCLUSIONS

This work describes the results of extensive investigations of MW-activated H_2 plasmas containing trace (10-100 ppm) amounts of SiH_4, with and without a few % of CH_4, operating at p and P values relevant to contemporary diamond CVD, using a combination of spatially resolved OE imaging and 2-D plasma

chemical modelling over a wide range of process conditions. The analysis and modelling of the OE from H*, H_2*, Si* (singlet and triplet) and SiH* species in the dilute Si/H plasmas confirms the operation of fast H-shifting reactions which ensure that Si atoms are the most abundant silicon-containing species throughout the entire reactor volume. The low ionization potentials of all SiH_x ($x \leq 4$) species (*cf.* the ionization potentials of H and H_2) and the efficiency of the ion conversion reactions ensure that even small SiH_4 additions will cause a change in the dominant ions in the plasma (from H_3^+ to SiH_x^+), with knock-on consequences for the electron-ion recombination rates and ambipolar diffusion coefficients. Other hitherto unrecognised complexities revealed by the present experimental / modelling study of dilute Si/H plasmas operating at high T_{gas} include the findings that the both EIE and CL reactions contribute to the observed ^{1}Si*, ^{3}Si* and SiH* emissions, that the high concentrations of ground state Si atoms throughout the reactor volume can attenuate the ^{3}Si* OE emanating from the hot plasma region and that the total silicon content in the reactor volume can be affected by silicon deposition at the reactor walls and the etching (by H atoms) of such deposits. Trace SiH_4 additions to a pre-existing C/H plasma are shown to cause only minor perturbations to the well-established C/H plasma chemistry. The presence of a few % CH_4 in the process gas mixture greatly reduces the H atom densities in the cooler regions of the reactor, and thus the efficiency of the H-atom induced shift from $SiH_4 \rightarrow$ Si in these regions. This, in turn, ensures that re-absorption of ^{3}Si* emission emanating from the hot plasma region is much reduced, and that OE measurements of ^{1}Si* or ^{3}Si* atoms should provide a reliable measure of the Si content in the core of a MW-activated Si/C/H plasma – a key requirement for growers who aspire to apply OE measurements for process control. The study confirms prior realizations that a Si substrate or fused silica components within a MW reactor (*e.g.* windows or a bell-jar) can be a ready source of gas phase Si-containing species and determines that Si atoms and/or SiC_2 species are likely to be the most abundant gas phase Si-containing species just above the growing diamond surface and thus the most likely carriers of the silicon incorporated in CVD diamond.

ASSOCIATED CONTENT

Supporting Information

The following Supporting Information is available free of charge on the ACS Publications website at DOI: [ACS to add]: Spatial distributions of H_2*(d-a) and H* (Balmer-γ) emissions from MW-activated SiH_4/H_2 plasmas as functions of p and P; time evolving spatial distributions of H* (Balmer-γ) and Si* emissions from a MW-activated H_2/(Ar) plasma operating above a Si substrate; further 2-D modelling results pertaining to Si/H plasmas; optical emission images from Si/C/H plasma operating under base conditions.

AUTHOR INFORMATION

Corresponding Authors

*E-mail: mike.ashfold@bristol.ac.uk; ymankelevich@mics.msu.su

ORCID

Michael N.R. Ashfold: 0000-0001-5762-7048

Yuri A Mankelevich: 0000-0002-7383-1396

Notes

The authors declare no competing financial interests.

All underlying data are available at the University of Bristol data repository, data.bris, at

https://doi.org/10.5523/bris.3fb2ydne4072k2rz6uhtyqo1gj.

Acknowledgements

The Bristol authors are grateful for financial support from the Engineering and Physical Sciences Research Council (EPSRC) through grant no. EP/K018388/1, the EPSRC Centre for Doctoral Training in Diamond Science and Technology (EP/L015315/1) and Element Six Ltd, and for technical help and support from Dr James Smith. The work was performed within the Cooperation in Science and Technology Agreement between Lomonosov Moscow State University, Skobeltsyn Institute of Nuclear Physics, and the University of Bristol.

Table 1

Species and Transitions Monitored by Optical Emission Imaging. The Si* Transitions are all part of the $3s^2 3p4s \rightarrow 3s^2 3p^2$ Multiplet. Term Values and Einstein A-Coefficients are from the Following Sources: Atomic Si and H,[56] SiH,[57,58] H_2,[54,59,60] CH [60-62] and C_2,[63] and the Diatomic Term Energies are for the Respective v = 0 Levels.

Species	**Transition**	E_{upper} **/ eV**	E_{lower} **/ eV**	**λ / nm**	A **/ 10^7 s^{-1}**
Si*	$^3P_2{}^o \rightarrow {}^3P_1$	4.95	0.01	250.69	5.47
Si*	$^3P_1{}^o \leftrightarrow {}^3P_0$	4.93	0	251.43	7.39
Si*	$^3P_2{}^o \rightarrow {}^3P_2$	4.95	0.03	251.61	16.8
Si*	$^3P_1{}^o \rightarrow {}^3P_1$	4.93	0.01	251.92	5.49
Si*	$^3P_0{}^o \leftrightarrow {}^3P_1$	4.91	0.01	252.41	22.2
Si*	$^3P_1{}^o \leftrightarrow {}^3P_2$	4.92	0.03	252.85	9.04
Si*	$^1P_1{}^o \rightarrow {}^1D_2$	5.08	0.78	288.16	21.7
Si*	$^1P_1{}^o \rightarrow {}^1S_0$	5.08	1.91	390.55	1.33
SiH*	$A^2\Delta \rightarrow X^2\Pi$	3.00	0	409-425	0.187
H*	$n = 5 \rightarrow n = 2$	13.05	10.20	434.05	~0.94
H*	$n = 4 \rightarrow n = 2$	12.75	10.20	486.13	~2.06
H_2*	$d^3\Pi_u \rightarrow a^3\Sigma_g^+$	13.97	11.79	600-615	2.57
CH*	$B^2\Sigma^- \rightarrow X^2\Pi$	3.208	0	380-390	0.307
CH*	$A^2\Delta \rightarrow X^2\Pi$	2.876	0	420-440	0.187
C_2*	$d^3\Pi_g \rightarrow a^3\Pi_u$	2.48	0.088	460-565	0.763

Table 2

Most Important Production/Loss Reactions *i* (and Rate Coefficients k_i) for SiH* and ^{1}Si* Species in a MW activated Si/H Plasma. Reaction Rates R_i (in $cm^{-3}s^{-1}$) are Presented for the Base Regime (*i.e.* p = 150 Torr, P = 1.5 kW, 48 ppm SiH_4 in H_2) and the following Conditions in the Plasma Core at r = 0, z = 10.5 mm: T_{gas} = 3080 K, T_e = 1.36 eV, Averaged Reduced Electric Field = 33.4 Td, Electron Density, $n_e = 3.4\times10^{11}$ cm^{-3} and H Atom Concentration, [H] = 4.7×10^{16} cm^{-3}. The Rate Coefficients, k_i, are in Units of $cm^3\,s^{-1}$ Except for the Radiative Decays (for which the Units are s^{-1}). T_{gas} is in K, T_e is in eV, and H_2, H and Si Denote the Respective Ground States.

i	**Reaction**	**Rate Coefficient, k_i**	**R_i / cm^{-3} s^{-1}**
H-Shifting Reactions			
1a	$SiH + H \leftrightarrow Si + H_2$	$1.2\times10^{-15}\times T_{gas}^{1.65}$	1.78×10^{19}
1b	$SiH + H \leftrightarrow Si + H_2$	$(2.92\times10^{-8}/T_{gas}^{0.7})\exp(-500/T_{gas})$	2.32×10^{18}
2	$^1SiH_2 + H \leftrightarrow SiH + H_2$	$(1.5\times10^{-6}/T_{gas})\exp(-800/T_{gas})$	1.85×10^{18}
3	$SiH_3 + H \leftrightarrow {}^1SiH_2 + H_2$	$(1.17\times10^{-9}/T_{gas}^{0.2})\exp(-180/T_{gas})$	2.99×10^{16}
4	$SiH_4 + H \leftrightarrow SiH_3 + H_2$	$2.79\times10^{-11}\exp(-1243/T_{gas})$	1.51×10^{14}
5	$SiH_3 + H \leftrightarrow {}^3SiH_2 + H_2$	$9.43\times10^{-18}\times T_{gas}^{2.28}\exp(-765/T_{gas})$	8.96×10^{16}
6	$SiH + H \leftrightarrow Si(^1D_2) + H_2$	$(1.84\times10^{-10}/T_{gas}^{0.18})\exp(-223/T_{gas})$	1.05×10^{18}
Electron Impact Ionization of SiH_x and Ion Conversion and Recombination Reactions			
7	$Si + e \rightarrow Si^+ + 2e$	$4.5\times10^{-8}\exp(-8.8/T_e)$	1.12×10^{14}
8	$Si(^1D_2) + e \rightarrow Si^+ + 2e$	$5.5\times10^{-8}\ T_e^{0.3}\exp(-8/T_e)$	7.79×10^{12}
9	$SiH + e \rightarrow SiH^+ + 2e$	$2.1\times10^{-8}\exp(-8.6/T_e)$	7.26×10^{12}
10	$H_3^+ + Si \leftrightarrow SiH^+ + H_2$	3.7×10^{-9}	9.25×10^{14}
11	$H_3^+ + SiH \leftrightarrow SiH_2^+ + H_2$	2.0×10^{-9}	5.89×10^{13}
12	$SiH^+ + H \rightarrow Si^+ + H_2$	1.9×10^{-9}	9.01×10^{18}
−12	$Si^+ + H_2 \rightarrow SiH^+ + H$	$1.62\times10^{-8}\exp(-15032/T_{gas})$	9.89×10^{18}
13	$H_3^+ + e \rightarrow H + 2H/H_2$	$4.5\times10^{-9}/T_e^{0.66}$	6.67×10^{13}
14	$SiH^+ + e \rightarrow H + Si(^1D_2)/Si(^1S_0)$	$8.7\times10^{-9}/T_e^{0.63}$	2.47×10^{14}
SiH* Production/Loss Reactions			
15	$SiH + e \rightarrow SiH^* + e$	$9.5\times10^{-9}T_e^{0.5}\exp(-3.7/T_e)$	1.43×10^{14}
16	$SiH^* \rightarrow SiH + h\nu$	1.87×10^{6}	3.35×10^{13}
17	$Si(^1D_2) + H_2 \rightarrow SiH^* + H$	$3.48\times10^{-9}\exp(-41045/T_{gas})$	3.09×10^{14}

17a	$^1SiH_2 + H \rightarrow SiH^* + H_2$	$3.15\times10^{-11}\exp(-19467/T_{gas})$	2.91×10^{14}
17b	$^3SiH_2 + H \rightarrow SiH^* + H_2$	$1.1\times10^{-11}\exp(-8261/T_{gas})$	2.91×10^{14}
–17	$SiH^* + H \rightarrow Si(^1D_2) + H_2$	5.0×10^{-10}	4.18×10^{14}
–17a	$SiH^* + H_2 \rightarrow {}^1SiH_2 + H$	5.0×10^{-11}	4.05×10^{14}
–17b	$SiH^* + H_2 \rightarrow {}^3SiH_2 + H$	5.0×10^{-11}	4.05×10^{14}
^{1}Si* and ^{3}Si* Production/Loss Reactions			
18	$Si + e \rightarrow {}^1Si^* + e$	$5.0\times10^{-10}\exp(-5.05/T_e)$	1.84×10^{13}
19	$Si(^1D_2) + e \rightarrow {}^1Si^* + e$	$1.7\times10^{-9}\exp(-4.23/T_e)$	3.09×10^{12}
20	$SiH^+ + e \rightarrow {}^1Si^* + H$	$2.7\times10^{-9}/T_e^{0.63}$	7.80×10^{13}
21	$^3Si^* + H \rightarrow {}^1Si^* + H$	$2.0\times10^{-9}\exp(-1996/T_{gas})$	1.40×10^{13}
–21	$^1Si^* + H \rightarrow {}^3Si^* + H$	6.0×10^{-9}	4.10×10^{13}
22	$^1Si^* + H_2 \rightarrow SiH + H$	5.0×10^{-10}	3.08×10^{13}
23	$^1Si^* + H \rightarrow SiH^+ + e$	$6.0\times10^{-9}\exp(-6340/T_{gas})$	5.24×10^{12}
24	$^1Si^* \rightarrow Si(^1D_2) + h\nu$	2.17×10^{8}	3.17×10^{13}
25	$^1Si^* \rightarrow Si(^1S_0) + h\nu$	1.33×10^{7}	1.94×10^{12}
26	$Si + e \rightarrow {}^3Si^* + e$	$2.0\times10^{-9}\exp(-4.9/T_e)$	8.25×10^{14}
27	$SiH^+ + e \rightarrow {}^3Si^* + H$	$9.1\times10^{-10}/T_e^{0.63}$	2.60×10^{13}
28	$^3Si^* + H_2 \rightarrow SiH + H$	5.0×10^{-10}	6.04×10^{13}
29	$^3Si^* + H \rightarrow SiH^+ + e$	$6.0\times10^{-9}\exp(-6340/T_{gas})$	1.03×10^{13}
30	$^3Si^* \rightarrow Si + h\nu$	2.21×10^{8}	6.34×10^{13}

Table 3.

Most Important Si/C/H Interconversion and Coupling Reactions *i*, with the Respective Forward (k_i) and Reverse (k_{-i}) Rate Coefficients (in $cm^3\ s^{-1}$) Assumed in the Present Modeling of a MW Activated 0.01%SiH_4/0.33%CH_4/H_2 Gas Mixture. The Final Two Columns show the Forward (R_i) and Reverse (R_{-i}) Reaction Rates (in $cm^{-3}\ s^{-1}$) Prevailing for the Base Regime (*i.e.* p = 150 Torr, P = 1.5 kW) and the Following Conditions in the Plasma Core at r = 0, z = 10.5 mm: T_{gas} = 3164 K, T_e = 1.3 eV, Averaged Reduced Electric Field = 31 Td, H Atom Concentration, [H] = 6.4×10^{16} cm^{-3}, Electron Density, $n_e = 4.3\times10^{11}$ and the More Abundant Ion Densities: [Si^+] = 1.5×10^{11}, [$C_2H_3^+$] = 1.4×10^{11}, [SiH^+] = 6.3×10^{10}, [SiC_2H^+] = 5×10^{10}, [H_3^+] = 1.5×10^{10} and [$C_2H_2^+$] = 8.3×10^9 cm^{-3}.

i	**Reaction**	k_i	k_{-i}		
	Ion Conversion Reactions			$R_i/10^{14}$	$R_{-i}/10^{14}$
31	$H_3^+ + Si \leftrightarrow SiH^+ + H_2$	3.7×10^{-9}	$7.0\times10^{-10}\exp(-49900/T_{gas})$	6.36	0.03
32	$SiH^+ + H \leftrightarrow Si^+ + H_2$	1.9×10^{-9}	$1.62\times10^{-8}\exp(-15032/T_{gas})$	8.8×10^4	9.6×10^4
33	$H_3^+ + C_2H_2 \leftrightarrow C_2H_3^+ + H_2$	1.94×10^{-9}	$3.98\times10^{-10}\exp(-25878/T_{gas})$	89.7	78.3
34	$C_2H_2^+ + Si \leftrightarrow SiC_2H^+ + H$	2.0×10^{-10}	$1.25\times10^{-11}\exp(-39771/T_{gas})$	0.16	0.002
35	$C_2H_3^+ + Si \leftrightarrow SiC_2H_2^+ + H$	2.0×10^{-10}	$1.25\times10^{-9}\exp(-12484/T_{gas})$	2.84	0.33
36	$Si^+ + C_2H_2 \leftrightarrow SiC_2H^+ + H$	2.5×10^{-11}	$5.99\times10^{-13}\exp(-2162/T_{gas})$	9.64	9.21
37	$Si^+ + C_2H \leftrightarrow SiC_2^+ + H$	1.0×10^{-9}	$1.27\times10^{-9}\exp(-3829/T_{gas})$	14.1	13.5
38	$SiC_2H_2^+ + H \leftrightarrow SiC_2H^+ + H_2$	2.0×10^{-10}	$5.53\times10^{-12}\exp(-28663/T_{gas})$	2.64	0.13
39	$SiC_2^+ + H_2 \leftrightarrow SiC_2H^+ + H$	1.5×10^{-9}	$4.38\times10^{-10}\exp(-12310/T_{gas})$	284	284
	Si/C Coupling Reactions			$R_i/10^{16}$	$R_{-i}/10^{16}$
40	$SiC_2H + H \leftrightarrow Si + C_2H_2$	1.0×10^{-10}	$3.47\times10^{-10}\exp(-8587/T_{gas})$	5.29	5.28
41	$Si(^1D) + C_2H_2 \leftrightarrow SiC_2H + H$	1.0×10^{-10}	$1.62\times10^{-11}\exp(-812/T_{gas})$	0.64	0.64
42	$SiH + C_2H_2 \leftrightarrow SiC_2H_2 + H$	5.0×10^{-11}	$2.0\times10^{-9}\exp(-2530/T_{gas})$	1.01	1.01
43	$Si + C_2H \leftrightarrow SiC_2 + H$	2.7×10^{-10}	$2.75\times10^{-9}\exp(-20888/T_{gas})$	1.79	1.79
44	$SiH + C_2H \leftrightarrow SiC_2H + H$	2.2×10^{-10}	$3.75\times10^{-9}\exp(-22975/T_{gas})$	0.14	0.14
	H-Shifting Reactions for SiC_2H_x Family (x = 0–2)			$R_i/10^{16}$	$R_{-i}/10^{16}$
45	$SiC_2H_2 + H \leftrightarrow SiC_2H + H_2$	1.0×10^{-10}	$2.43\times10^{-12}\exp(-6266/T_{gas})$	0.11	0.11
46	$SiC_2H + H \leftrightarrow SiC_2 + H_2$	1.0×10^{-10}	$3.88\times10^{-10}\exp(-16710/T_{gas})$	5.29	5.29

Figure Captions

Figure 1

(a) $I_{em}(\lambda, z)$ image in the wavelength range $372 \leq \lambda \leq 447$ nm recorded from a MW-activated Si/H plasma operating under base conditions. Panel (b) shows the corresponding $I_{em}(\lambda)$ plot obtained by summing all emission in the height range $10.5 \leq z \leq 12$ mm and wavelength range $410 \leq \lambda \leq 425$ nm and its decomposition into components attributable to SiH*, H_2* and Si* transitions. Most of the structure in the spectrum labelled residual (in blue), obtained as the difference between the measured spectrum (in black) and the PGOPHER simulated SiH(A-X) spectrum (in red) matches that in the spectrum from the corresponding SiH_4-free H_2 plasma (in mauve), and can be assigned to H_2* emissions. The one remaining line in the black trace at λ ~411.6 nm is a spin-forbidden Si* transition discussed in the text.

Figure 2

$I_{em}(\lambda, z)$ images recorded in the wavelength ranges (a) $252 \leq \lambda \leq 327$ nm and (c) $463 \leq \lambda \leq 534$ nm from a MW-activated Si/H plasma operating under base conditions. The corresponding $I_{em}(\lambda)$ plots obtained by summing all emission in the range $10.5 \leq z \leq 12$ mm within the more limited ranges $270 \leq \lambda \leq 310$ nm and $470 \leq \lambda \leq 510$ nm are shown in panels (b) and (d), respectively. Note that all the Si* lines in (d) are appearing in second order; the fundamental wavelengths of these transitions are all at half the displayed *x*-axis value.

Figure 3

Spatial distributions of H_2*(d-a), H* (Balmer-γ), SiH* and the various Si* emissions from a MW-activated SiH_4/H_2 plasma operating under base conditions, normalised such that each distribution has the same peak intensity.

Figure 4

Spatial profiles of (a) $I_{em}(H_2^*)$, (b) $I_{em}(H^*)$, (c) $I_{em}(^3Si^*)$ and (d) $I_{em}(^1Si^*, 288\text{ nm})$ as functions of $F(SiH_4/H_2)$ with all other parameters held at their values under base conditions. The black curve in each case shows the profile for base conditions. Panel (e) shows how the summed intensity of each emitter in a limited spatial range ($9 \leq z \leq 12$ mm for $I_{em}(H^*)$, $I_{em}(^3Si^*)$ and $I_{em}(^1Si^*)$, $0 \leq z \leq 3$ mm for $I_{em}(H_2^*)$) varies with $F(SiH_4/H_2)$, each normalised to unity at base conditions.

Figure 5

Spatial profiles of (a) $I_{em}(^3Si^*)$, (b) $I_{em}(^1Si^*, 288\text{ nm})$ and (c) $I_{em}(SiH^*)$ as functions of total pressure, *p*, with all other parameters held at conditions. The black curve in each case shows the profile for base conditions. Panel (d) shows how the summed intensity of each emitter in the limited range $9 \leq z \leq 12$ mm varies with *p*, each normalised to unity at base conditions (*i.e.* $p = 150$ Torr).

Figure 6

Spatial profiles of (a) $I_{em}(^3Si^*)$, (b) $I_{em}(^1Si^*, 288\ nm)$ and (c) $I_{em}(SiH^*)$ as functions of MW power, P, with all other parameters held at conditions. The black curve in each case shows the profile for base conditions. Panel (d) shows how the summed intensity of each emitter in the limited range $9 \leq z \leq 12$ mm varies with P, each normalised to unity at base conditions (*i.e.* $P = 1.5$ kW).

Figure 7

Radial profiles (r, $z = 10.5$ mm) of the calculated concentrations of (a) neutral Si-containing species and (b) H atoms and the more abundant ions under base reactor conditions. Panel (b) also shows the corresponding gas (T_{gas}) and electron (T_e) temperature profiles under these reactor conditions (right hand vertical axis).

Figure 8

Calculated $\{SiH^*, v=0\}(z)$ column densities as functions of (a) $X_0(SiH_4)$, (b) p and (c) P (with, in both cases, $X_0(SiH_4) = 48$ ppm), compared with the measured $I_{em}(SiH^*, z)$ profiles (where available), with all other parameters maintained at their base values.

Figure 9

Calculated SiH* production (*i.e.* $SiH + e \rightarrow SiH^* + e$; (15) and $Si(^1D_2) + H_2 \rightarrow SiH^* + H$; (17)) and loss (*i.e.* $SiH^* \rightarrow SiH + h\nu$; (16) and $SiH^* + H \rightarrow Si(^1D_2) + H_2$; (−17)) reaction rate profiles (for $r = 0$, z) at p = (a) 60, (b) 150 and (c) 250 Torr at base $P = 1.5$ kW and $X_0(SiH_4) = 48$ ppm.

Figure 10

Comparisons between calculated $\{^1Si^*\}(z)$ column densities and measured $I_{em}(^1Si^*, 288\ nm, z)$ profiles as functions of (a) $X_0(SiH_4)$, (b) p and (c) P with, in each case, all other parameters maintained at their base values.

Figure 11

Spatial profiles of (a) $I_{em}(H_2^*)$ and (b) $I_{em}(H^*)$ upon adding CH_4 to a pre-existing Si/H plasma operating under the base conditions of $X_0(SiH_4)$, p and P. Panel (c) shows the $F(CH_4)$-dependences of the $I_{em}(H_2^*, 0 \leq z \leq 3\ mm)$, $I_{em}(H^*, 6 \leq z \leq 9\ mm)$, $I_{em}(CH^*, 9 \leq z \leq 12\ mm)$ and $I_{em}(C_2^*, 9 \leq z \leq 12\ mm)$ in the specified height ranges. Each trace has been normalised to a common intensity of 1 at $F(CH_4) = 1$ sccm apart from that for $I_{em}(C_2^*)$ where, for display purposes, the intensity at $F(CH_4) = 1$ sccm has been set at 0.25.

Figure 12

Spatial profiles of (a) $I_{em}(H_2^*)$ and (b) $I_{em}(H^*)$ upon adding SiH_4 to a pre-existing C/H plasma operating with $F(CH_4) = 19$ sccm and at base conditions of p and P. Panel (c) shows the $F(CH_4)$-dependences of the $I_{em}(H_2^*, 0 \leq z \leq 3\ mm)$, $I_{em}(H^*, 6 \leq z \leq 9\ mm)$ and $I_{em}(CH^*)$, $I_{em}(C_2^*)$, $I_{em}(^3Si^*)$, $I_{em}(^1Si^*, 288\ nm)$

– two separate experiments – and I_{em}(SiH*) all in the height range $9 \leq z \leq 12$ mm, with each trace normalised to a common intensity at $F(SiH_4/H_2)$ = 30 sccm.

Figure 13

Spatial profiles of (a) $I_{em}(^3Si^*)$ and (b) $I_{em}(^1Si^*, 288\ nm)$ upon adding CH_4 to a pre-existing Si/H plasma operating under the base conditions of $X_0(SiH_4)$, p and P. (Note some of the intermediate traces have been omitted from (a) to avoid over-cluttering the figure). (c) Comparison of the $I_{em}(^3Si^*)$, $I_{em}(^1Si^*)$ and I_{em}(SiH*) profiles recorded under base conditions intensities and normalised to a common peak intensity. (d) $F(CH_4)$-dependences of the summed intensities of $I_{em}(^3Si^*)$ and $I_{em}(^1Si^*, 288\ nm)$ – two separate experiments – and I_{em}(SiH*) in the range $9 \leq z \leq 12$ mm, each normalised to the same relative intensity at $F(CH_4)$ = 1 sccm.

Figure 1

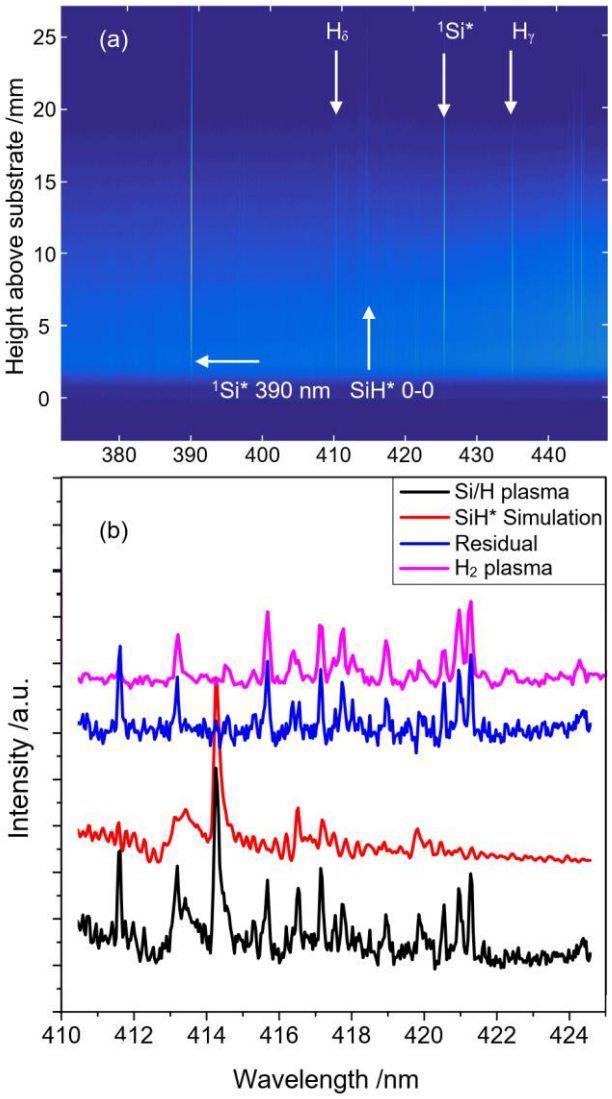
(a)
H_δ
$^1Si^*$
H_γ
Height above substrate /mm
25
20
15
10
5
0
380
390
400
410
420
430
440
$^1Si^*$ 390 nm
SiH* 0-0
(b)
Si/H plasma
SiH* Simulation
Residual
H_2 plasma
Intensity /a.u.
410
412
414
416
418
420
422
424
Wavelength /nm

Figure 2

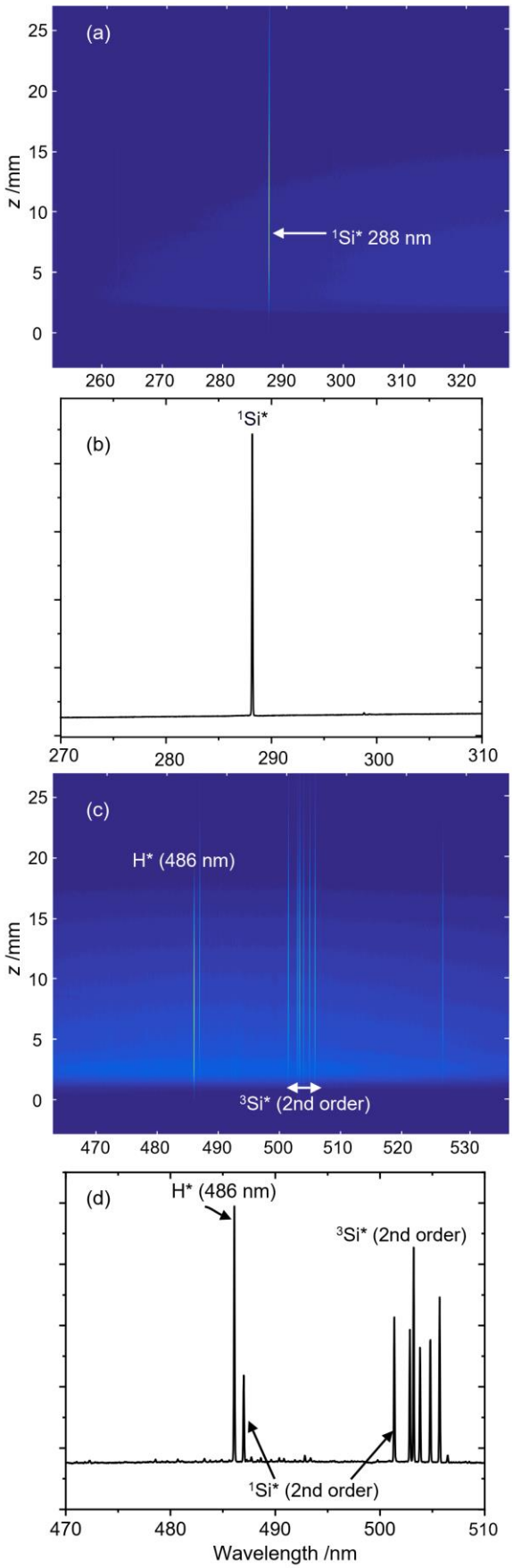
(a)
z /mm
^{1}Si* 288 nm
(b)
^{1}Si*
(c)
H* (486 nm)
^{3}Si* (2nd order)
(d)
H* (486 nm)
^{3}Si* (2nd order)
^{1}Si* (2nd order)
Wavelength /nm

Figure 3

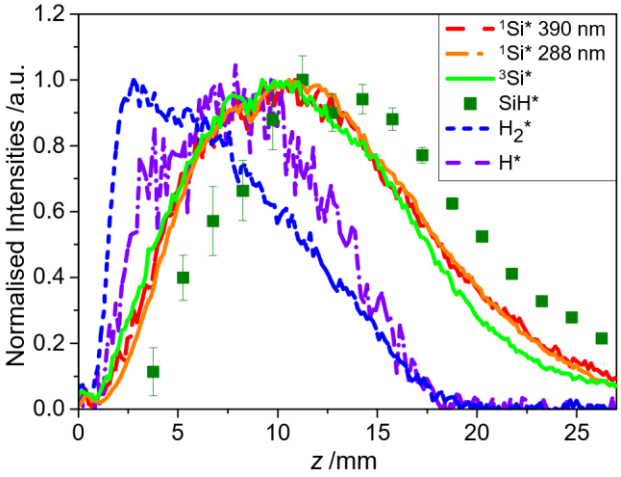
Normalised Intensities /a.u.
z /mm
1.2
1.0
0.8
0.6
0.4
0.2
0.0
0
5
10
15
20
25
¹Si* 390 nm
¹Si* 288 nm
³Si*
SiH*
H2*
H*

Figure 4

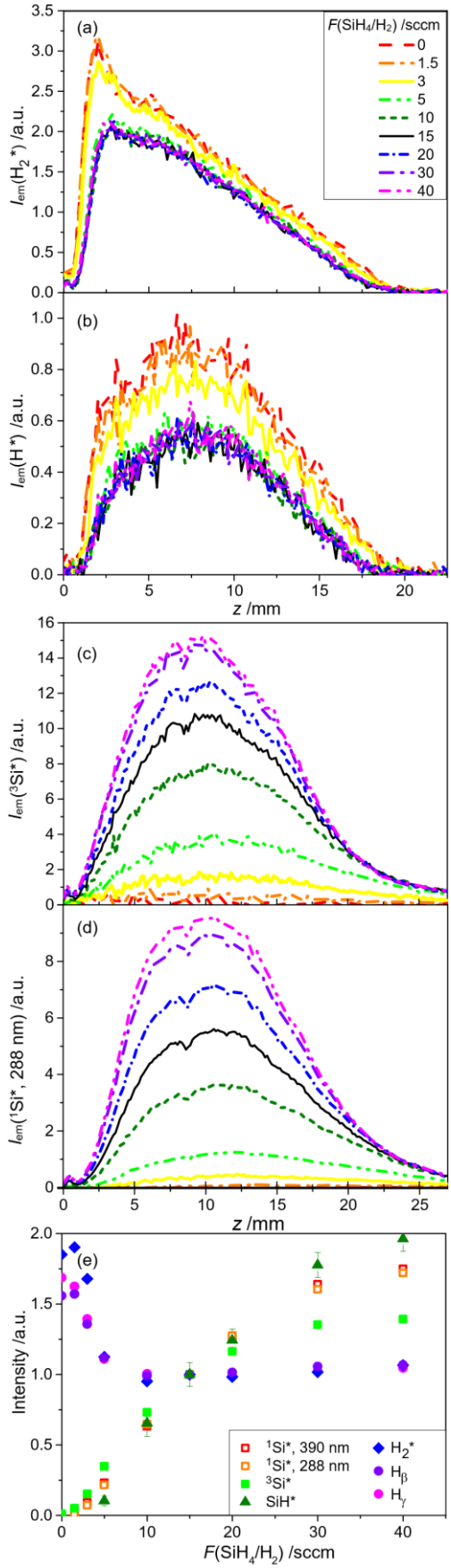
(a)
$F(SiH_4/H_2)$ /sccm
0
1.5
3
5
10
15
20
30
40
$I_{em}(H_2^*)$ /a.u.
(b)
$I_{em}(H^*)$ /a.u.
z /mm
(c)
$I_{em}(^3Si^*)$ /a.u.
(d)
$I_{em}(^1Si^*, 288\ nm)$ /a.u.
z /mm
(e)
Intensity /a.u.
$^1Si^*$, 390 nm
$^1Si^*$, 288 nm
$^3Si^*$
SiH*
H_2^*
H_β
H_γ
$F(SiH_4/H_2)$ /sccm

Figure 5

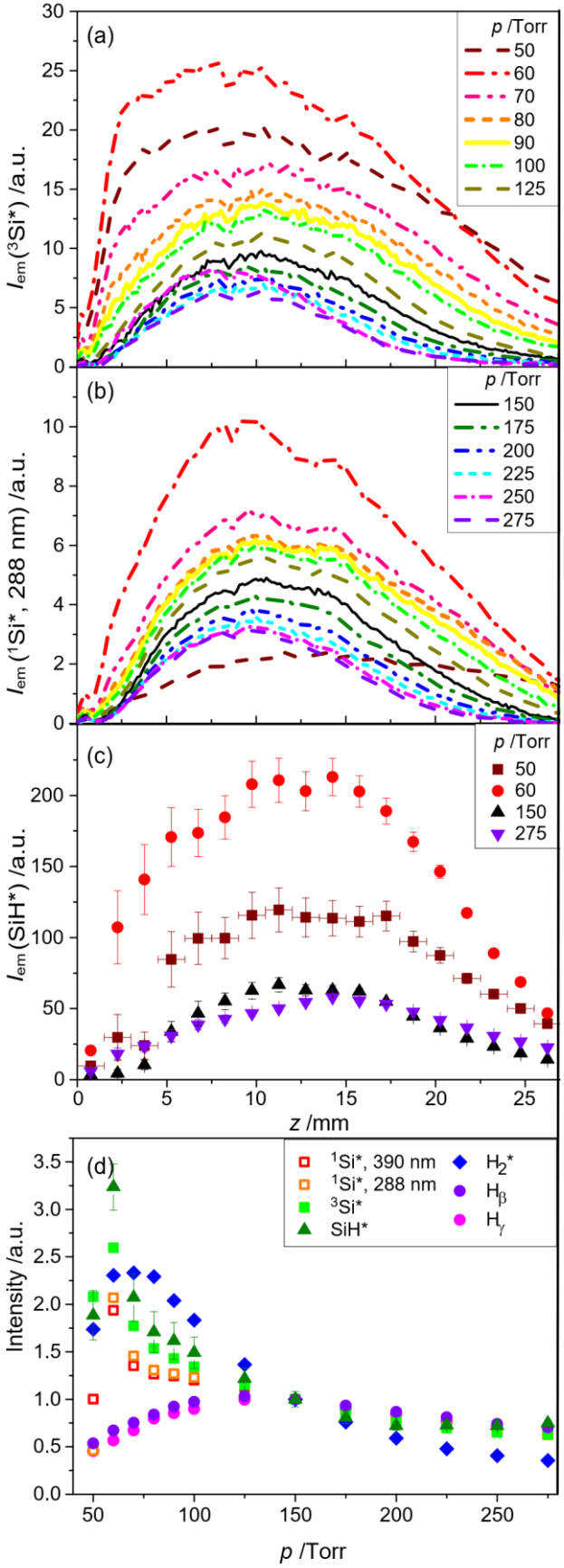
(a)
p /Torr
50
60
70
80
90
100
125
I_{em}(^{3}Si*) /a.u.
(b)
p /Torr
150
175
200
225
250
275
I_{em}(^{1}Si*, 288 nm) /a.u.
(c)
p /Torr
50
60
150
275
I_{em}(SiH*) /a.u.
z /mm
(d)
^{1}Si*, 390 nm
^{1}Si*, 288 nm
^{3}Si*
SiH*
H_2*
H_β
H_γ
Intensity /a.u.
p /Torr

Figure 6

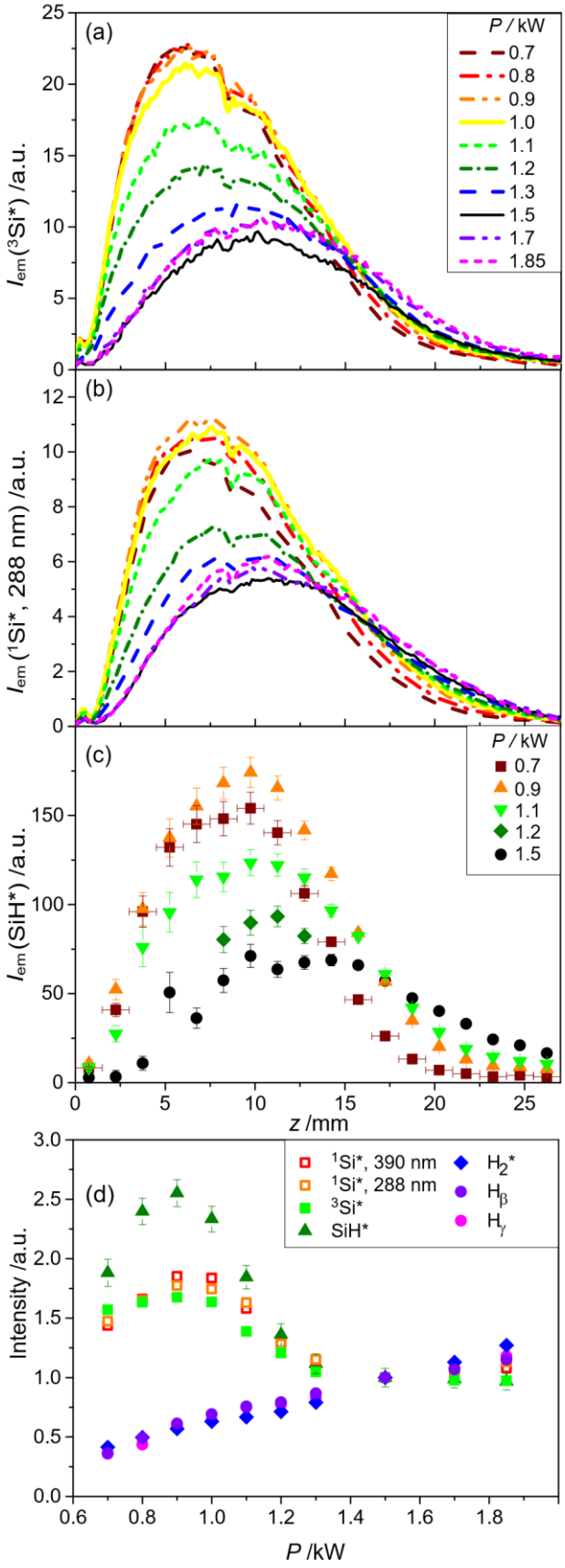
(a)
P / kW
0.7
0.8
0.9
1.0
1.1
1.2
1.3
1.5
1.7
1.85
I_em(3Si*) /a.u.
(b)
I_em(1Si*, 288 nm) /a.u.
(c)
P / kW
0.7
0.9
1.1
1.2
1.5
I_em(SiH*) /a.u.
z /mm
(d)
1Si*, 390 nm
1Si*, 288 nm
3Si*
SiH*
H2*
Hβ
Hγ
Intensity /a.u.
P /kW

Figure 7

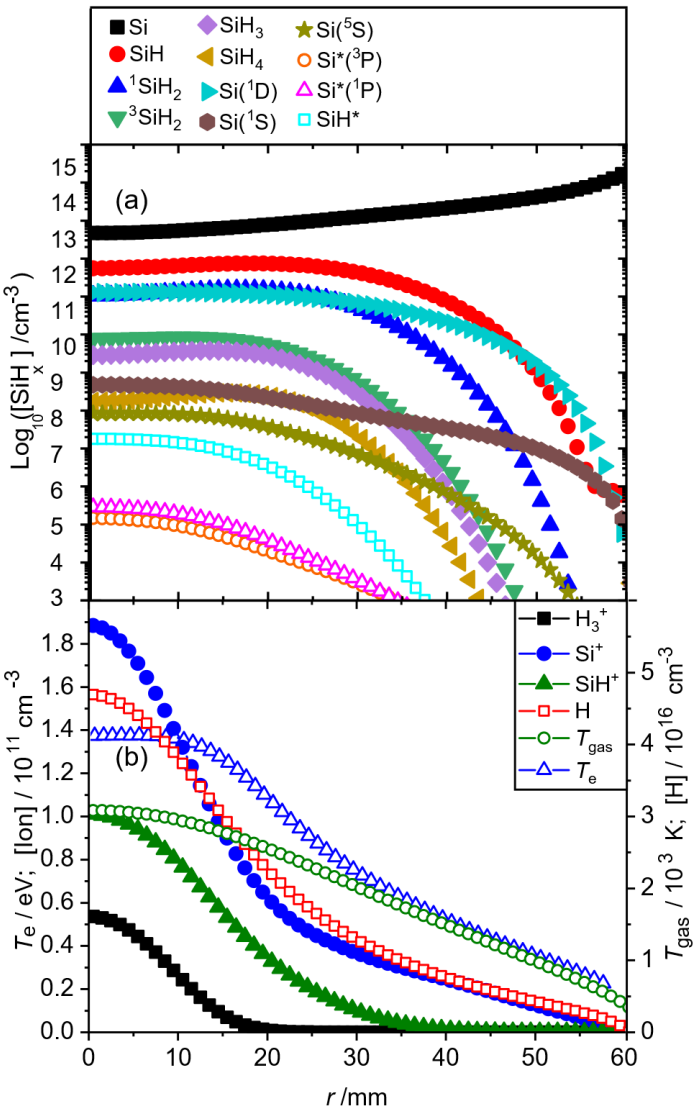
Si
SiH
1SiH2
3SiH2
SiH3
SiH4
Si(1D)
Si(1S)
Si(5S)
Si*(3P)
Si*(1P)
SiH*
(a)
Log10([SiHx] /cm-3)
(b)
H3+
Si+
SiH+
H
Tgas
Te
Te / eV; [Ion] / 10 11 cm-3
Tgas / 10 3 K; [H] / 10 16 cm-3
r /mm

Figure 8

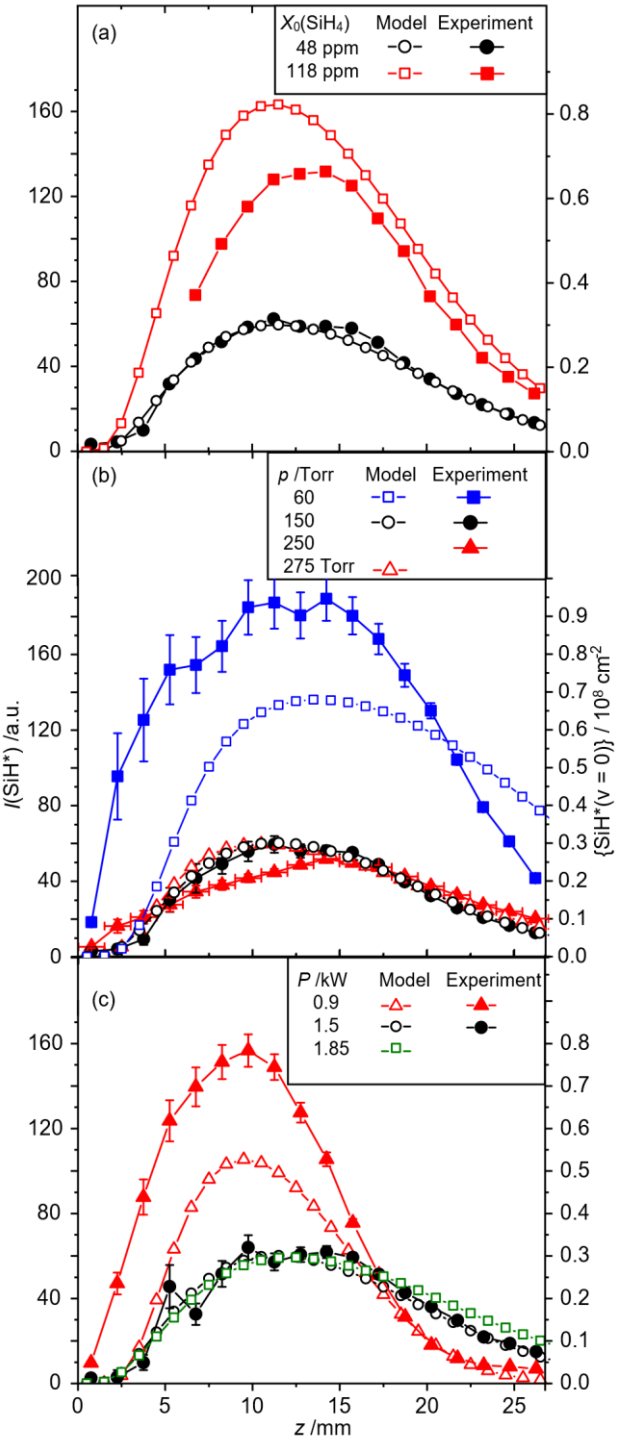
(a)
X0(SiH4) Model Experiment
48 ppm
118 ppm
(b)
p /Torr Model Experiment
60
150
250
275 Torr
(c)
P /kW Model Experiment
0.9
1.5
1.85
I(SiH*) /a.u.
{SiH*(v = 0)} / 10^8 cm^-2
z /mm

Figure 9

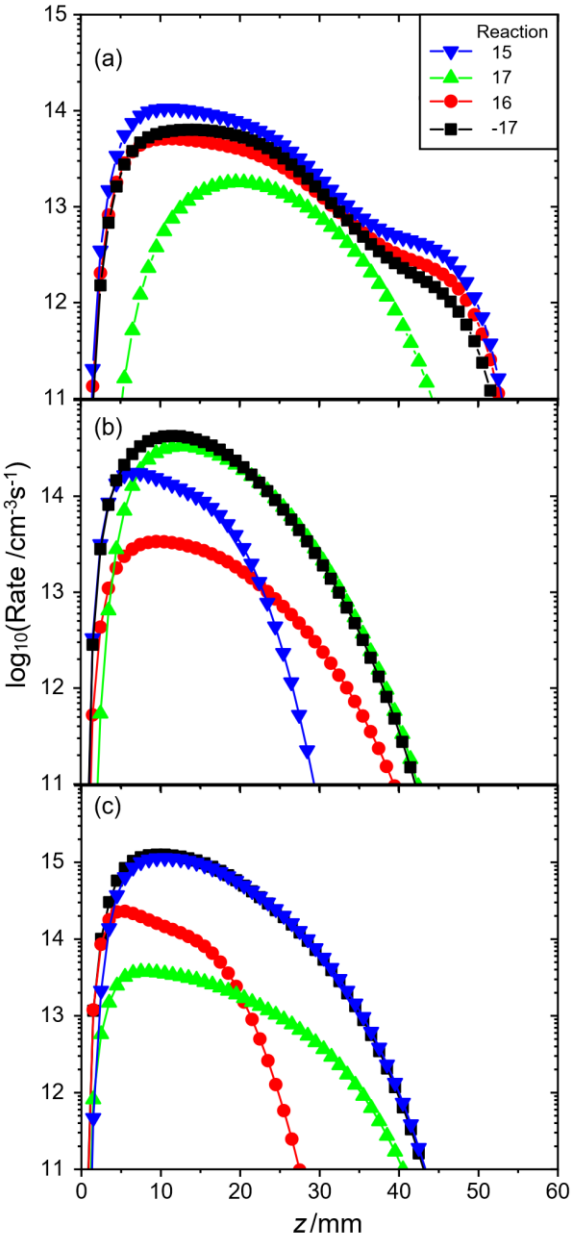

Figure 10

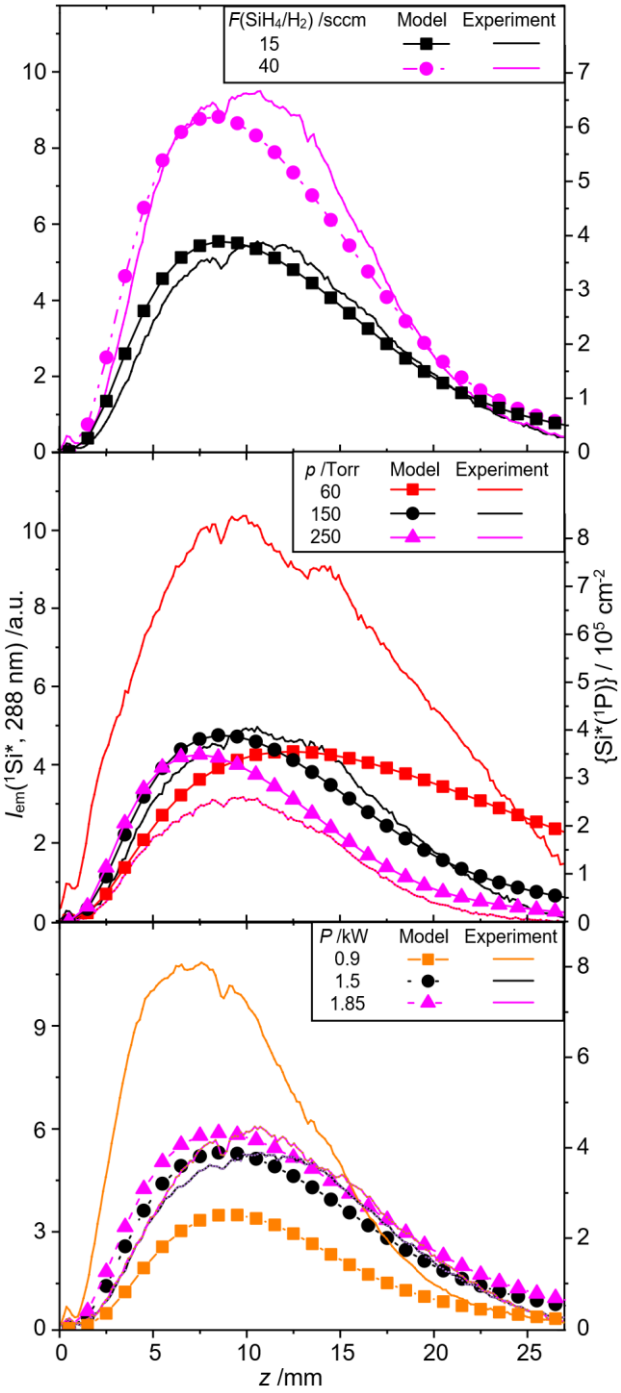
F(SiH4/H2) /sccm
15
40
Model
Experiment
p /Torr
60
150
250
P /kW
0.9
1.5
1.85
Iem(1Si*, 288 nm) /a.u.
{Si*(1P)} / 10^5 cm^-2
z /mm

Figure 11

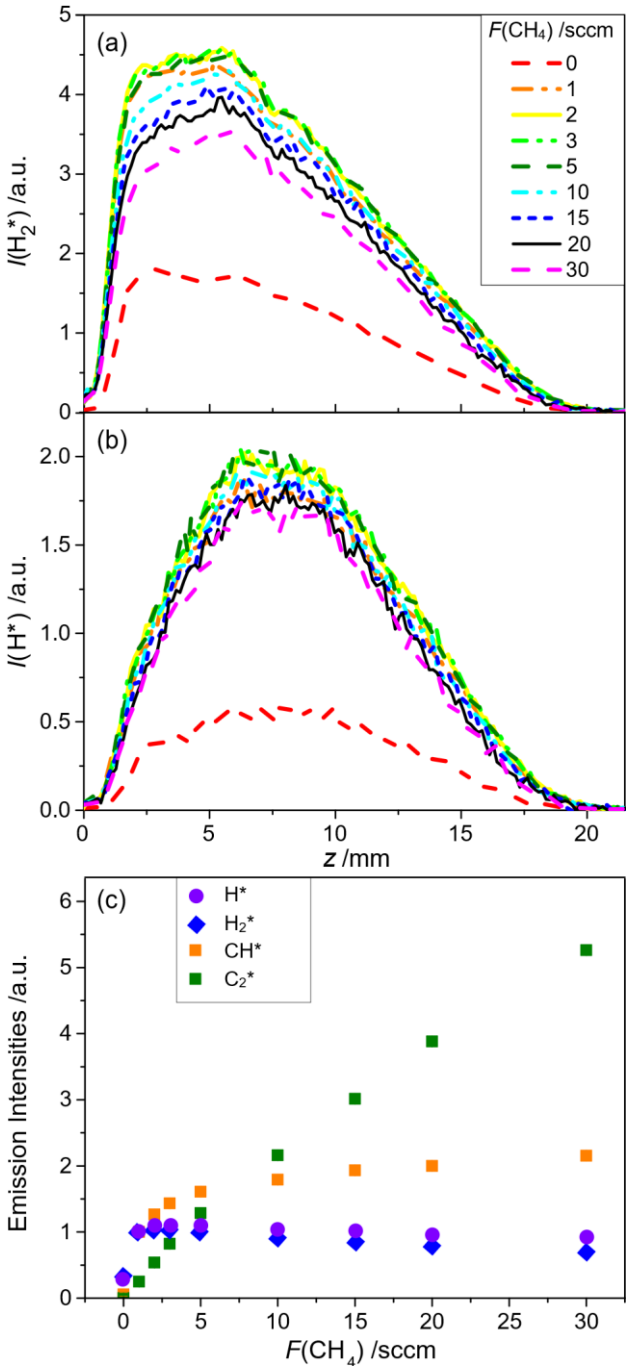
(a)
F(CH4) /sccm
0
1
2
3
5
10
15
20
30
I(H2*) /a.u.
(b)
I(H*) /a.u.
z /mm
(c)
H*
H2*
CH*
C2*
Emission Intensities /a.u.
F(CH4) /sccm

Figure 12

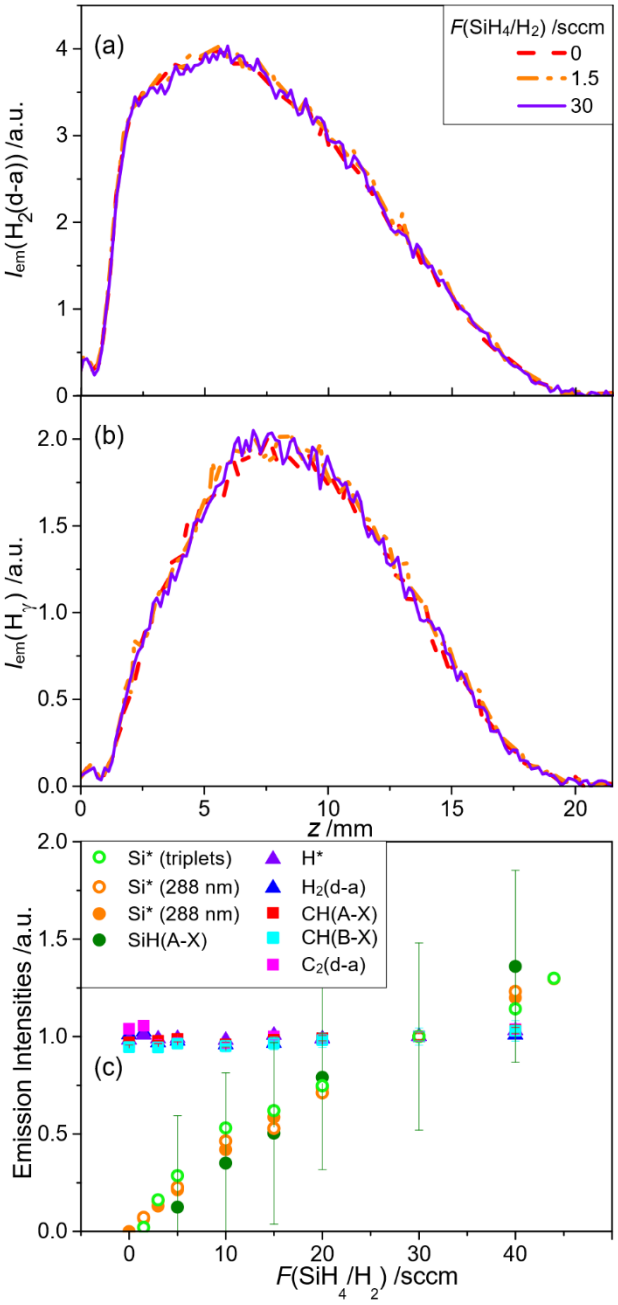
(a)
F(SiH4/H2) /sccm
0
1.5
30
Iem(H2(d-a)) /a.u.
(b)
Iem(Hγ) /a.u.
z /mm
(c)
Si* (triplets)
Si* (288 nm)
Si* (288 nm)
SiH(A-X)
H*
H2(d-a)
CH(A-X)
CH(B-X)
C2(d-a)
Emission Intensities /a.u.
F(SiH4/H2) /sccm

Figure 13

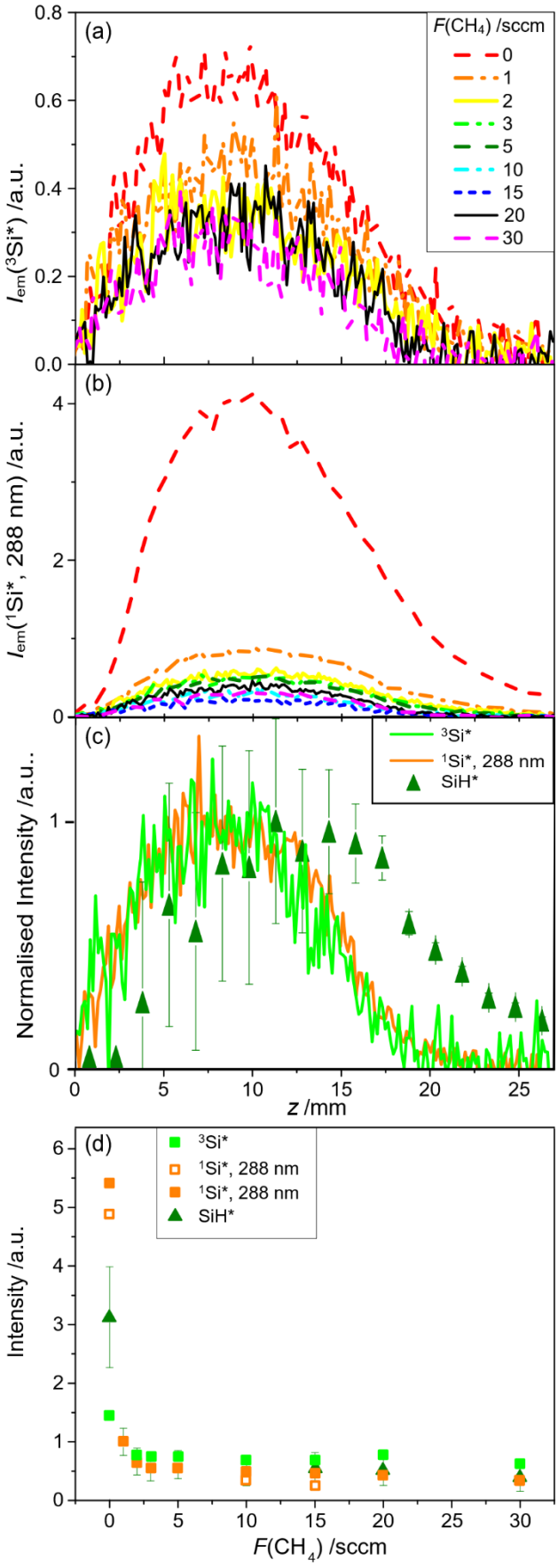
(a)
F(CH4) /sccm
0
1
2
3
5
10
15
20
30
Iem(3Si*) /a.u.
(b)
Iem(1Si*, 288 nm) /a.u.
(c)
3Si*
1Si*, 288 nm
SiH*
Normalised Intensity /a.u..
z /mm
(d)
3Si*
1Si*, 288 nm
1Si*, 288 nm
SiH*
Intensity /a.u.
F(CH4) /sccm

TOC Graphic

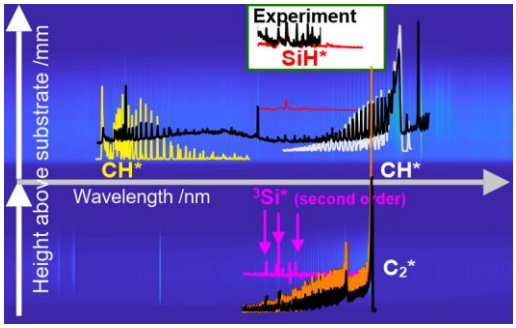
Experiment
SiH*
CH*
CH*
Wavelength /nm
Height above substrate /mm
^{3}Si* (second order)
C_2*

References

[1] Butler, J.E.; Mankelevich, Yu.A.; Cheesman, J.; Ma, J.; Ashfold, M.N.R. Understanding the Chemical Vapor Deposition of Diamond: Recent Progress. *J. Phys. Condens. Matter* **2009**, *21*, 364201.

[2] Ushizawa, K.; Watanabe, K.; Ando, T.; Sakaguchi, I.; Nishitani-Gamo, M.; Sato, Y.; Kanda, H. Boron Concentration Dependence of Raman Spectra on {100} and {111} Facets of B-Doped CVD Diamond. *Diam. Rel. Mater.* **1998**, *7*, 1719-1722.

[3] Bolshakov, A.; Ralchenko, V.; Sedov, V.; Khomich, A.; Vlasov, I.; Khomich, A.; Trofimov, N.; Krivobok, V.; Nikolaev, S.; Khmelnitskii, R.; *et al*. Photoluminescence of SiV Centers in Single Crystal CVD Diamond in situ Doped with Si from Silane. *Phys. Stat. Solidi A.* **2015**, *212*, 2525-2532.

[4] Sedov, V.: Ralchenko, V.; Khomich, A.A.; Vlasov, I.; Vul, A.; Savin, S.; Goryachev, A.; Konov, V.; Si-doped Nano- and Microcrystalline Diamond Films with Controlled Bright Photoluminescence of Silicon-Vacancy Color Centers, *Diam. Relat. Mater.* **2015**, *56*, 23-28.

[5] Ralchenko, V.G.; Sedov, V.S.; Martyanov, A.K.; Bolshakov, A.P.; Boldyrev, K.N.; Krivobok, V.S.; Nikolaev, S.N.; Bolshedvorskii, S.V.; Rubinas, O.R.; Akimov, A.V.; *et al*. Monoisotopic Ensembles of Silicon-Vacancy Color Centres with Narrow-Line Luminescence in Homoepitaxial Diamond Layers grown in H_2-CH_4-^{x}SiH_4 Gas Mixtures (x = 28, 29, 30). *ACS Photonics* **2019**, *6*, 66-72.

[6] Gicquel, A.; Silva, F.; Hassouni, K. Diamond Growth Mechanisms in Various Environments. *J. Electrochem. Soc.* **2000**, *147*, 2218-2226.

[7] Ma, J.; Ashfold, M N.R.; Mankelevich, Yu.A. Validating Optical Emission Spectroscopy as a Diagnostic of Microwave Activated CH_4/Ar/H_2 Plasmas used for Diamond Chemical Vapor Deposition. *J. Appl. Phys.* **2009**, *105*, 043302.

[8] Ma, J.; Richley, J. C.; Ashfold, M. N. R.; Mankelevich, Yu. A. Probing the Plasma Chemistry in a Microwave Reactor used for Diamond Chemical Vapor Deposition by Cavity Ring Down Spectroscopy. *J. Appl. Phys.* **2008**, *104*, 103305.

[9] Ashfold, M.N.R.; Mahoney, E.J.D.; Mushtaq, S.; Truscott, B.S.; Mankelevich, Yu.A. What [Plasma used for Growing] Diamond can Shine like Flame? *Chem. Comm.* **2017**, *53*, 10482-10495.

[10] Mankelevich, Yu.A.; Ashfold, M.N.R.; Ma. J. Plasma-Chemical Processes in Microwave Plasma-Enhanced Chemical Vapor Deposition Reactors Operating with C/H/Ar Gas Mixtures. *J. Appl. Phys*. **2008**, *104*, 113304.

[11] Ruan, J.; Choyke, W.J.; Partlow, W.D. Si Impurity in Chemical Vapor-Deposited Diamond Films. *Appl. Phys. Letts*. **1991**, *58*, 295-297.

[12] Turukhin, A.V.; Liu, C.H.; Gorokhovsky, A.A.; Alfano, R.R.; Phillips, W. Picosecond Photoluminescence Decay of Si-Doped Chemical-Vapor-Deposited Diamond Films. *Phys. Rev. B* **1996**, *54*, 16448-16451.

[13] Iakoubovskii, K.; Stesmans, A. Characterization of Hydrogen and Silicon-Related Defects in CVD Diamond by Electron Spin Resonance. *Phys. Rev. B*, **2002**, *66*, 195207.

[14] Singh, S.; Thomas, V.; Martyshkin, D.; Kozlovskaya, V.; Kharlampieva, E.; Catledge, S.A. Spatially Controlled Fabrication of a Bright Fluorescent Nanodiamond-Array with Enhanced Far-Red Si–V Luminescence. *Nanotechnol*. **2014**, *25*, 45302.

[15] Sedov, V.; Ralchenko, V.; Khomich, A.A.; Vlasov, I.; Vul, A.; Savin, S.; Goryachev, A.; Konov, V. Si-doped Nano- and Microcrystalline Diamond Films with Controlled Bright Photoluminescence of Silicon-Vacancy Color Centers. *Diam. Rel. Mater*. **2015**, *56*, 23-28.

[16] Felgen, N.; Naydenov, B.; Turner, S.; Jelezko, F.; Reithmaier, J.P.; Popov, C. Incorporation and Study of SiV Centers in Diamond Nanopillars." *Diam. Relat. Mater*. **2016**, *64*, 64-69.

[17] Ralchenko, V.G.; Sedov, V.S.; Saraykin, V.; Bolshakov, A.; Zavedeev, E.; Ashkinazi, E.; Khomich, A. Precise Control of Photoluminescence of Silicon-Vacancy Color Centers in Homoepitaxial Single-Crystal Diamond: Evaluation of Efficiency of Si Doping from Gas Phase. *Appl. Phys. A.* **2016**, *122*, 795.

[18] Ralchenko, V.G.; Sedov, V.S.; Martyanov, A.K.; Bolshakov, A.P.; Boldyrev, K.N.; Krivobok, V.S.; Nikolaev, S.N.; Bolshedvorskii, S.V.; Rubinas, O.R.; Akimov, A.V.; *et al.* Monoisotopic Ensembles of Silicon-Vacancy Color Centers with Narrow-Line Luminescence in Homoepitaxial Diamond Layers Grown in H_2-CH_4-$^xSiH_4$ Gas Mixtures (x = 28, 29, 30), *ACS Photonics* **2019**, *6*, 66–72.

[19] D'Haenens-Johansson, U.F.S.; Edmonds, A.M.; Green, B.L.; Newton, M.E.; Davies, G.; Martineau, P.M., Khan, R.U.A.; Twitchen, D.J. Optical Properties of the Neutral Split-Vacancy in Diamond. *Phys. Rev. B*. **2011**, *84*, 245208.

[20] Gali, A.; Maze, J.R. *Ab Initio* Study of the Split-Vacancy Defect in Diamond: Electronic Structure and Related Properties. *Phys. Rev. B*. **2013**, *88*, 235205.

[21] Jahnke, K.D.; Sipahigil, A.; Binder, J.M.; Doherty, M.W.; Metsch, M.; Rogers, L.J.; Manson, N.B.; Lukin, M.D.; Jelezko, F. Electron-Phonon Processes of the Silicon-Vacancy Centre in Diamond. *New. J. Phys*. **2015**, *17*, 043011.

[22] Green, B.L.; Doherty, M.W.; Nako, E.; Manson, N.B.; D'Haenens-Johansson, U.F.S.; Williams, S.D.; Twitchen, D.J.; Newton, M.E. Electronic Structure of the Neutral Silicon-Vacancy Center in Diamond. *Phys. Rev. B*. **2019**, *99*, 161112.

[23] Hepp, C.; Muller, T.; Waselowski, V.; Becker, J.N.; Pingault, B.; Sternschulte, H.; Steinmüller-Nethl, D.; Gali, A.; Maze, J.R.; Atatüre, M.; *et al.* Electronic Structure of the Silicon Vacancy Color Center in Diamond. *Phys. Rev. Letts*. **2014**, *112*, 036405.

[24] Rogers, L.J.; Jahnke, K.D.; Metsch, M.H.; Sipahigil, A.; Binder, J.M.; Teraji, T.; Sumiya, H.; Isoya, J.; Lukin, M.D.; Hemmer, P.; *et al*. All-Optical Initialization, Readout, and Coherent Preparation of Single Silicon-Vacancy Spins in Diamond. *Phys. Rev. Letts*. **2014**, *113*, 263602.

[25] Becker, J.N.; Gorlitz, J.; Arend, C.; Markham, M.; Becher, C. Ultrafast All-Optical Coherent Control of Single Vacancy Colour Centres in Diamond. *Nat. Comm*. **2016**, *7*, 13512.

[26] Sipahigil, A.; Evans, R.E.; Sukachev, D.D.; Burek, M.J.; Borregaard, J.; Bhaskar, M.K.; Nguyen, C.T.; Pacheco, J.L.; Atikian, H.A.; Meuwly, C.; *et al*. An Integrated Diamond Nanophotonics Platform for Quantum-Optical Networks. *Science* **2016**, *354*, 847.

[27] Sukachev, D.D.; Sipahagil, A.; Nguyen, C.T.; Bhaskar, M.K.; Evans, R.E.; Jelezko, F.; Lukin, M.D. Silicon-Vacancy Spin Qubit in Diamond: A Quantum Memory Exceeding 10 ms with Single-Shot State Readout. *Phys. Rev. Letts*. **2017**, *119*, 223602.

[28] Becker, J.N.; Pingault, B.; Gross, S.; Gundogan, M.; Kukharchyk, N.; Markham, M.; Edmonds, A.; Atature, M.; Bushey, P.; Becher, C. All-Optical Control of the Silicon-Vacancy Spin in Diamond at Millikelvin Temperatures, *Phys. Rev. Letts.* **2018**, *120*, 053603.

[29] Lemonde, M.-A.; Meesala, S.; Sipahigil, A.; Schuetz, M.J.A.; Lukin, M.D.; Loncar, M.; Rabl, P. Phonon Networks with Silicon-Vacancy Centers in Diamond Waveguides. *Phys. Rev. Letts*. **2018**, *120*, 213603.

[30] Meesala, S.; Sohn, Y.-I.; Pingault, B.; Shao, L.B.; Atikian, H.A.; Holzgrafe, J.; Gundogan, M.; Stavrakas, C.; Sipahigil, A.; Chia, C.; *et al*. Strain Engineering of the Silicon-Vacancy Center in Diamond. *Phys. Rev. B*. **2018**, *97*, 205444.

[31] Evans, R.E.; Bhaskar, M.K.; Sukachev, D.D.; Nguyen, C.T.; Sipahigil, A.; Burek, M.J.; Machielse, B.; Zhang, G.H.; Zibrov, A.S.; Bielejec, E.; *et al*., Photon-Mediated Interactions Between Quantum Emitters in a Diamond Nanocavity. *Science* **2018**, *362*, 662-665.

[32] Weinzetl, C.; Gorlitz, J.; Becker, J.N.; Walmsley, J.A.; Poem, E.; Nunn, J.; Becher, C. Coherent Control and Wave Mixing in an Ensemble of Silicon-Vacancy Centers in Diamond. *Phys. Rev. Lett.* **2019**, *122*, 063601.

[33] Haussler, S.; Benedikter, J.; Bray, K.; Regan, B.; Dietrich, A.; Twamley, J.; Aharonovich, I.; Hunger, D.; Kubanek, A. Diamond Photonics Platform based on Silicon Vacancy Centers in a Single-Crystal Diamond Membrane and a Fiber Cavity. *Phys. Rev. B*. **2019**, *99*, 165310.

[34] Metsch, M.H.; Senkalla, K.; Tratzmiller, B.; Scheuer, J.; Kern, M.; Achard, J.; Tallaire, A.; Plenio, M.B.; Siyushev, P.; Jelezko, F. Initialization and Readout of Nuclear Spins via a Negatively Charged Silicon-Vacancy Center in Diamond. *Phys. Rev. Letts*. **2019**, *122*, 190503.

[35] Merson, T.D.; Castelletto, S.; Aharonovich, I.; Turbic, A.; Kilpatrick, T.J.; Turnley, A.M. Nanodiamonds with Silicon Vacancy Defects for Nontoxic Photostable Fluorescent Labeling of Neural Precursor Cells. *Opt. Letts*. **2013**, *38*, 4170-4173.

[36] Bray, K.; Cheung, L.; Hossain, R.; Aharonovich, I.; Valenzuela, S.M., Shimoni, O. Versatile Multicolor Nanodiamond Probes for Intracellular Imaging and Targeted Labeling. *J. Mater. Chem. B* **2018**, *6*, 3078-3084.

[37] Choi, S.M.; Agafonov, V.N.; Davydov, V.A.; Plakhotnik, T. Ultrasensitive All-Optical Thermometry Using Nanodiamonds with a High Concentration of Silicon-Vacancy Centers and Multiparametric Data Analysis. *ACS Photonics* **2019**, *6*, 1387-1392.

[38] Green, B.L.; Doherty, M.W.; Nako, E.; Manson, N.B.; D'Haenens-Johansson, U.F.S.; Williams, S.D.; Twitchen, D.J.; Newton, M.E. Electronic Structure of the Neutral Silicon-Vacancy Center in Diamond. *Phys. Rev. B*. **2019**, *99*, 161112.

[39] Shah, A.V.; Schade, H.; Vanecek, M.; Meier, J.; Vallat-Sauvain, E.; Wyrsch, N.; Kroll, U.; Droz, C.; Bailat, J. Thin-Film Silicon Solar Cell Technology. *Prog. Photovoltaics* **2004**, *12*, 113-142.

[40] Mauk, M.; Sims, P.; Rand, J.; Barnett, A. Thin Silicon Solar Cells in *Practical Handbook of Photovoltaics* (2nd edn.), Academic Press. **2012**, 161-206. ISBN 9780123859341

[41] Koh, J.; Ferlauto, A.S.; Rovira, P.I.; Wronski, C.R.; Collins, R.W. Evolutionary Phase Diagrams for Plasma-Enhanced Chemical Vapor Deposition of Silicon Thin Films from Hydrogen-Dilute Silane. *Appl. Phys. Letts*. **1999**, *75*, 2286-2288.

[42] Strahm, B.; Howling, A.A.; Sansonnens, L.; Hollenstein, Ch. Plasma Silane Concentration as a Determining Factor for the Transition from Amorphous to Microcrystalline Silicon in SiH_4/H_2 Discharges. *Plasma Sources Sci. Technol*. **2007**, *16*, 80-89.

[43] Kortshagen, U. Nonthermal Plasma Synthesis of Semiconductor Nanocrystals. *J. Phys. D: Appl. Phys*. **2009**, *42*, 113001.

[44] Sahu, B.B.; Han, J.G.; Shin, K.S.; Ishikawa, K.; Hori, M.; Miyawaki, Y. Plasma Diagnostic Approach for High Rate Nanocrystalline Si Synthesis in RF/UHF Hybrid Plasmas Using a PECVD Process. *Plasma Sources Sci. Technol*. **2015**, *24*, 025019.

[45] Shindo, W.; Sakai, S.; Tanaka, H.; Zhong, C.J.; Ohmi, T. Low-Temperature Large-Grain Poly-Si Direct Deposition by Microwave Plasma Enhanced Chemical Vapor Deposition Using SiH_4/Xe. *J. Vac. Sci. Technol. A* **1999**, *17*, 3134-3138.

[46] Wrobel, A.M.; Walkiewicz-Pietrzykowska, A.; Ahola, M.; Vayrynen, I.J.; Ferrer-Fernandez, F.J.; Gonzalez-Elipe, A. Growth Mechanism and Chemical Structure of Amorphous Hydrogenated Silicon Carbide (a-SiC:H) Films Formed by Remote Hydrogen Microwave Plasma CVD from a Triethylsilane Precursor: Part 1. *Chem. Vap. Depos*. **2009**, *15*, 39-46.

[47] Jiang, X.; Klages, C.P. Synthesis of Diamond β-SiC Composite Films by Microwave Plasma Assisted Chemical Vapor-Deposition. *Appl. Phys. Letts*. **1992**, *61*, 1629-1631.

[48] Zhuang, H.; Zhang, L.; Staedler, T.; Jiang, X. Highly Selective Diamond and β-SiC Crystal Formation at Increased Atomic Hydrogen Concentration: A Route for Synthesis of High-Quality and Patterned Hybrid Diamond/β-SiC Composite Film. *Scripta Mater*. **2011**, *65*, 548-551.

[49] Sedov, V.S.; Martyanov, A.K.; Khomich, A.A.; Savin, S.S.; Voronov, V.V.; Khmelnitskiy, R.A.; Bolshakov, A.P.; Ralchenko, V.G. Co-Deposition of Diamond and β-SiC by Microwave Plasma CVD in H_2-CH_4-SiH_4 Gas Mixtures. *Diam. Rel. Mater*. **2019**, *98*, 107520.

[50] Jasinski, J.M.; Becerra, R.; Walsh, R. Direct Kinetic-Studies of Silicon Hydride Radicals in the Gas-Phase. *Chem. Rev*. **1995**, *95*, 1203-1228.

[51] Raghunath, P.; Lee, Y.; Wu, S.; Wu, J.; Lin, M. Ab Initio Chemical Kinetics for Reactions of H Atoms with SiH_x(x = 1-3) Radicals and Related Unimolecular Decomposition Processes. *Int. J. Quant. Chem*. **2013**, *113*, 1735-1746.

[52] Stinespring, C.D.; Wormhoudt, J.C. Gas Phase Kinetics Analysis and Implications for Silicon Carbide Chemical Vapor Deposition. *J. Cryst. Growth*, **1988**, *87*, 481-493.

[53] Allendorf, M.D.; Kee, R.J. A Model of Silicon Carbide Chemical Vapor Deposition, *J. Electrochem. Soc*. **1991**, *138*, 841-852.

[54] Mahoney, E.J.D.; Truscott, B.S.; Mushtaq, S.; Ashfold, M.N.R.; Mankelevich, Yu.A. Spatially Resolved Optical Emission and Modeling Studies of Microwave-Activated Hydrogen Plasmas Operating under Conditions Relevant for Diamond Chemical Vapor Deposition. *J. Phys. Chem. A* **2018**, *122*, 8286-8300.

[55] Mahoney, E.J.D.; Rodriguez, B.J.; Mushtaq, S.; Truscott, B.S.; Ashfold, M.N.R.; Mankelevich, Yu.A. Imaging and Modelling the Optical Emission from CH Radicals in Microwave Activated C/H Plasmas *J. Phys. Chem. A* **2019**, *123*, 9966-9977.

[56] Kramida, A.; Ralchenko, Yu.; Reader, J. and NIST ASD Team (2018). *NIST Atomic Spectra Database* (version 5.6.1), https://physics.nist.gov/asd [retrieved Thursday August 22, 2019]. National Institute of Standards and Technology, Gaithersburg, MD. DOI: https://doi.org/10.18434/T4W30F.

[57] Ram, R.S.; Engleman, R.; Bernath, P.F. Fourier Transform Emission Spectroscopy of the $A^2\Delta$–$X^2\Pi$ Transition of SiH and SiD. *J. Mol. Spect*. **1998**, *190*, 341-352.

[58] Bauer, W.; Becker, K.H.; Düren, R.; Bubrich, C.; Meuser, R. Radiative Lifetime Measurements of SiH($A^2\Delta$) by Laser Induced Fluorescence. *Chem. Phys. Lett*. **1984**, *108*, 560-561.

[59] Dieke, G.H. The Molecular Spectrum of Hydrogen and its Isotopes. *J. Mol. Spectrosc*. **1958**, *2*, 494−517 and references therein.

[60] Huber, K.P.; Herzberg, G. Constants of Diatomic Molecules (data prepared by J.W. Gallagher and R.D. Johnson, III) in NIST Chemistry WebBook, NIST Standard Reference Database Number 69, Eds. P.J. Linstrom and W.G. Mallard, National Institute of Standards and Technology, Gaithersburg MD, 20899, https://doi.org/10.18434/T4D303, (retrieved Thursday August 22, 2019).

[61] Luque, J.: Crosley, D.R. Electronic Transition Moment and Rotational Transition Probabilities in CH. 1. $A^2\Delta$ - $X^2\Pi$ System. *J. Chem. Phys*. **1996**, *104*, 2146-2155.

[62] Luque, J.: Crosley, D.R. Electronic Transition Moment and Rotational Transition Probabilities in CH. 2. $B^2\Sigma^-$–$X^2\Pi$ System. *J. Chem. Phys*. **1996**, *104*, 3907-3913.

[63] Brooks, J.; Bernath, P.; Schmidt, T.; Bacskay, G. Line Strengths and Updated Molecular Constants for the C_2 Swan System. *J. Quant. Spectrosc. Radiat. Transfer* **2013**, *124*, 11-20.

[64] Western C.M. PGOPHER, A Program for Simulating Rotational, Vibrational and Electronic Spectra, *J. Quant. Spectrosc. Rad. Trans*. **2017**, *186*, 221-242.

[65] Mahoney, E.J.D. Alternative Excitation Mechanisms Occurring within Microwave-Activated Plasmas under Conditions Relevant to the Chemical Vapour Deposition of Diamond. Ph.D. Thesis, University of Bristol, 2019.

[66] Mahoney, E.J.D.; Mushtaq, S.; Ashfold, M.N.R.; Mankelevich, Yu. A. Combined Spatially Resolved Optical Emission Imaging and Modelling Studies of Microwave-Activated H_2/Ar and H_2/Kr Plasmas Operating at Powers and Pressures Relevant for Diamond Chemical Vapor Deposition. *J. Phys. Chem. A*, **2019**, *123*, 2544-2558.

[67] Vepřek, S.; Schopper K.; Ambacher, O.; Rieger, W.; Veprek-Heijman, M.G.J. Mechanism of Cluster Formation in a Clean Silane Discharge. *J. Electrochem. Soc.* **1993**, *140*, 1935-1942.

[68] Mironovich, K.V.; Mankelevich, Yu.A.; Voloshin, D.G.; Dagesjan, S.A.; Krivchenko, V.A. Modeling and Optical Spectroscopy of DC Discharge in $CH_4/H_2/N_2$ Mixture for Nanostructured Carbon Films. *Plasma Physics Reports*. **2017**, *43*, 839-852.

[69] Ma, J.; Richley, J.C.; Davies, D.R.W.; Cheesman, A.; Ashfold, M.N.R.; Mankelevich, Yu.A. Spectroscopic and Modeling Investigations of the Gas-Phase Chemistry and Composition in Microwave Plasma Activated $B_2H_6/Ar/H_2$ Mixtures. *J. Phys. Chem. A* **2010**, *114*, 2447–2463.

[70] Ma, J.; Richley, J.C.; Davies, D.R.W.; Ashfold, M.N.R.; Mankelevich, Yu.A. Spectroscopic and Modeling Investigations of the Gas Phase Chemistry and Composition in Microwave Plasma Activated $B_2H_6/CH_4/Ar/H_2$ Mixtures. *J. Phys. Chem. A.* **2010**, *114*, 10076–10089.

[71] Truscott, B.S.; Kelly, M.W.; Potter, K.J.; Johnson, M.; Ashfold, M.N.R.; Mankelevich, Yu.A. Microwave Plasma-Activated Chemical Vapor Deposition of Nitrogen-Doped Diamond. I. N_2/H_2 and NH_3/H_2 Plasmas. *J. Phys. Chem. A* **2015**, *119*, 12962-12976.

[72] Berkowitz, J.; Greene, J.P.; Cho, H.; Ruščic, Photoionization Mass Spectrometric Studies of SiH_n (n=1-4). *J. Chem. Phys.* **1987**, *86*, 1235-1248.

[73] Burcat, A.; Goos. E. Ideal Gas Thermochemical Properties of Silicon containing Inorganic, Organic Compounds, Radicals, and Ions. *Int. J. Chem. Kin*. **2018**, *50*, 633-650.

[74] Kim, Y.-K.; Stone, P.M. Ionization of Silicon, Germanium, Tin and Lead by Electron Impact. *J. Phys. B: At. Mol. Opt. Phys.* **2007**, *40*, 1597–1611.

[75] Tarnovsky, V.; Deutsch, H.; Becker. K. Electron Impact Ionization of the SiD_x (x =1–3) Free Radicals. *J. Chem. Phys.* **1996**, *105*, 6315-6321.

[76] Millar, T.J.; Farquhar, P.R.A.; Willacy, P.K. The UMIST Database for Astrochemistry 1995. *Astron. Astrophys., Suppl. Ser.* **1997**, *121*, 139−185.

[77] Larsson, M.; McCall, B.J.; Orel, A.E. The Dissociative Recombination of H_3^+ – A Saga Coming to an End? *Chem. Phys. Lett.* **2008**, *462*, 145-151.

[78] Janev, R.K.; Reiter, D. Collision Processes of Hydride Species in Hydrogen Plasmas: III. The Silane Family. Contrib. Plasma Phys. **2003**, *43*, 401-417.

[79] Perrin, J.; Delafosse, E. Emission-Spectroscopy of SiH in a Silane Glow-Discharge *J. Phys. D – Appl. Phys*. **1980**, *13*, 759-765.

[80] Stamou, S.; Matara, D.; Rapakoulias, D. Simulation of the SiH($A^2\Delta$–$X^2\Pi$) Emission Spectrum in a Silane Glow Discharge and Derivation of an Improved Set of Molecular Constants. *Chem. Phys*. **1997**, *218*, 57-69.

[81] Kessels, W.M.M.; van de Sanden, M.C.M.; Schram, D.C. Film Growth in a Remote SiH_4 Plasma used for High-Rate Deposition of Hydrogenated Amorphous Silicon. *J. Vac. Sci. Technol. A* **2000**, *18*, 2153-2163.

[82] Baranov, E.A.; Khmel, S.Ya. Simulation of the Emission Spectrum of SiH($A^2\Delta \rightarrow X^2\Pi$) and Measurement of the Rotational Temperature of the $A^2\Delta$ State in an Electron-Beam Plasma. *J. Appl. Mech. Tech. Phys*. **2003**, *44*, 605-611.

[83] Moon, S.Y.; Kim, W.Y.; Lee, H.C.; Ahn, S.W.; Lee, H.M.; Choe, W. Measurement of Rotational Temperature using SiH($A^2\Delta$–$X^2\Pi$) Emission Spectrum in SiH_4-H_2 Plasmas. *Phys. Plasmas* **2010**, *17*, 083501.

[84] Marvi, Z.; Xu, S.; Foroutan, G.; Ostrikov, K.; Levchenko, I. Plasma-Deposited Hydrogenated Amorphous Silicon Films: Multiscale Modelling Reveals Key Processes. *RSC Adv*. **2017**, *7*, 19189-19196.

[85] Wanka, H.N.; Schubert, M.B. High Silicon Etch Rates by Hot Filament Generated Atomic Hydrogen. *J. Phys. D: Appl. Phys.* **1997**, *30*, L28–L31.

[86] Husain, D.; Norris, P.E. Kinetic Study of Reactions of Ground State Silicon Atoms, Si[$3p^2(^3P_J)$], by Atomic Absorption Spectroscopy. *J. Chem. Soc. Farad. Trans. 2*, **1978**, *74*, 106-114.

[87] Husain, D.; Norris, P.E. Collisional Quenching of Electronically Excited Silicon Atoms, Si[$3p^2(^1D_2)$], by Atomic Absorption Spectroscopy. *J. Chem. Soc. Farad. Trans. 2*, **1978**, *74*, 1483-1503.

[88] Basu, S.C.; Husain, D. Measurement of Absolute Rate Data for the Reactions of Ground-State Atomic Silicon Si(3^3P_J) with Acetylenes by Time-Resolved Atomic Resonance-Absorption Spectroscopy. *J. Photochem. Photobiol. A* **1988**, *42*, 1-12.

[89] Canosa, A.; Le Picard, S.D.; Gougeon, S.; Rebrion-Rowe, C.; Travers, D.; Rowe, B.R. Rate Coefficients for the Reactions of Si(^3P_J) with C_2H_2 and C_2H_4: Experimental results down to 15 K. *J. Chem. Phys.* **2001**, *115*, 6495-6503.

[90] Smith, I.W.M.; Sage, A.M.; Donahue, N.M.; Herbst, E.; Quan, D. The Temperature-Dependence of Rapid Low Temperature Reactions: Experiment, Understanding and Prediction. *Faraday Discuss*. **2006**, *133*, 137-156.

[91] Talbi, D. An Extensive *Ab Initio* Study of the Si + C_2H_2 and Si + C_2H_4 Reactions in Relation to the Silicon Astrochemistry. *Chem. Phys*. **2005**, *313*, 17-23.

[92] Kaiser, R.I.; Krishtal, S.P.; Mebel, A.M.; Kostko, O.; Ahmed, M. An Experimental and Theoretical Study of the Ionization Energies of SiC_2H_x (x = 0, 1, 2) Isomers. *Astrophys. J.* **2012**, *76*, 178 and references therein.

[93] Kaiser, R.I.; Gu, X. Chemical Dynamics of the Formation of the Ethynylsilylidyne Radical (SiCCH($X^2\Pi$)) in the Crossed Beam Reaction of Ground State Silicon Atoms (Si(^3P)) with Acetylene ($C_2H_2(X^1\Sigma_g^+)$). *J. Chem. Phys.* **2009**, *131*, 104311.

[94] Parker, D.S.N.; Wilson, A.V.; Kaiser, R.I.; Mayhall, N.J.; Head-Gordon, M.; Tielens, A.G.G.M. On the Formation of Silacyclopropenylidene (c-SiC_2H_2) and its Role in the Organosilicon Chemistry in the Interstellar Medium. *Astrophys. J.* **2013**, *770*, 33.

[95] Chase, M.W. Jr., NIST-JANAF Thermochemical Tables, Fourth Edition, *J. Phys. Chem. Ref. Data*, **1998**, *Monograph 9*, 1-1951.

[96] Ma, J.; Cheesman, A; Ashfold, M.N.R.; Hay, K.G.; Wright, S.; Langford, N; Duxbury, G.; Mankelevich, Yu.A. Quantum Cascade Laser Investigations of CH_4 and C_2H_2 Interconversion in Hydrocarbon/H_2 Gas Mixtures During Microwave Plasma Enhanced Chemical Vapor Deposition of Diamond. *J. Appl. Phys.* **2009**, *106*, 033305.